Geophysical Journal International

Geophys. J. Int. (2015) **200,** 596–614
GJI Geodynamics and tectonics

doi: 10.1093/gji/ggu418

Lithospheric mantle heterogeneities beneath the Zagros Mountains and the Iranian Plateau: a petrological-geophysical study

Lavinia Tunini, Ivone Jiménez-Munt, Manel Fernandez, Jaume Vergés and Antonio Villaseñor

Group of Dynamics of the Lithosphere, Institute of Earth Sciences Jaume Almera, ICTJA-CSIC, Barcelona, Spain. E-mail: ltunini@ictja.csic.es

Accepted 2014 October 24. Received 2014 October 13; in original form 2014 February 17

SUMMARY

We apply a combined geophysical-petrological methodology in order to study the thermal, compositional, density and seismological structure of the crust and upper mantle along two transects across the Arabia–Eurasia collision region. Results on the crustal thickness show minimum values beneath the Arabia Platform and Central Iran (42–43 km), and maximum values beneath the Sanandaj Sirjan zone (SSZ; 55–63 km), in agreement with seismic data. Major discrepancies in Moho depth from those derived from seismic data are locally found in the SSZ (central Zagros) and Alborz Mountains where more moderate crustal thicknesses are modelled. Results on the lithosphere thickness indicate that the Arabian lithosphere is ∼220 km thick along both profiles, whereas Eurasian lithosphere is up to ∼90 km thinner, especially below the Central Iran and Alborz Mountains. The lithosphere–asthenosphere boundary (LAB) shows different geometries between the two transects. In the northern profile (northern Zagros), the LAB rises sharply below the SSZ in a narrow region of ∼90 km, whereas in the southern profile (central Zagros), rising occurs in wider region, from the Zagros fold-and-thrust belt (ZFTB) to the SSZ. The best fit of seismic velocities (*Vp*, *Vs*) and densities requires lateral changes in the lithospheric mantle composition. Our results are compatible with Proterozoic peridotitic mantle compositions beneath the Arabian Platform, Mesopotamian Foreland Basin and the accreted terrains of Eurasia Plate, and with a more depleted Phanerozoic harzburgitic-type mantle composition below the ZFTB and imbricated zone.

Key words: Gravity anomalies and Earth structure; Composition of the mantle; Continental margins: convergent.

1 INTRODUCTION

The Zagros Mountains are the result of the long-standing convergence between the Arabian Plate and Gondwana-derived tectonic fragments of the southern margin of the Eurasian Plate. The area has been the subject of numerous geophysical surveys and tectonic studies mainly focused on both the sedimentary cover and the basement units that configure the inner parts of the Zagros Mountains (Sanandaj Sirjan and Urumieh Dokhtar domains). During the last decade, many efforts have been devoted to unravelling the lithospheric structure and, particularly, in imaging the topography of the crust–mantle boundary (e.g. Paul *et al.* 2006, 2010; Gök *et al.* 2008; Gritto *et al.* 2008; Sodoudi *et al.* 2009; Manaman *et al.* 2011; see also Jiménez-Munt *et al.* 2012 for a thorough compilation on crustal thickness data).

Studies dealing with the subcontinental mantle structure are scarce and include global, regional and local teleseismic models (e.g. Maggi & Priestley 2005; Alinaghi *et al.* 2007, Kaviani *et al.* 2007; Manaman & Shomali 2010; see next sections for a more complete reference list). Results from these studies show fast mantle seismic velocities in the Arabian Plate and slower seismic velocities in Central Iran. Surface waveform tomography (Maggi & Priestley 2005) suggests a thin lithosphere beneath the Turkish–Iranian plateau probably related with partial delamination of an earlier thickened lithosphere. Tomographic cross-sections presented by Alinaghi *et al.* (2007) show northward-dipping high-velocity mantle anomalies beneath Central Iran, which can be interpreted as remnants of the subducted Neotethys oceanic lithosphere, as was later noted by Paul *et al.* (2010). Shomali *et al.* (2011) investigated the upper-mantle structure of the Zagros Mountains in southwest Iran, using traveltime teleseismic tomography. The results show a thick (more than 200 km) continental lithosphere in the Arabian Platform, while very thin (or no) lithospheric mantle is seen in Central Iran. The authors also noted the presence of a disconnected cold NE-dipping oceanic slab or detached mantle lithosphere beneath Central Iran, suggesting a lithospheric delamination below the main Zagros fault (MZF).

The lithospheric mantle thinning below the Iranian Plateau was also proposed during the 1970s–1980s from earthquake distribution and focal mechanisms (Bird 1978) and from gravity and flexural studies (Snyder & Barazangi 1986). Integrated 2-D models combining lithostatic, gravity and thermal equations

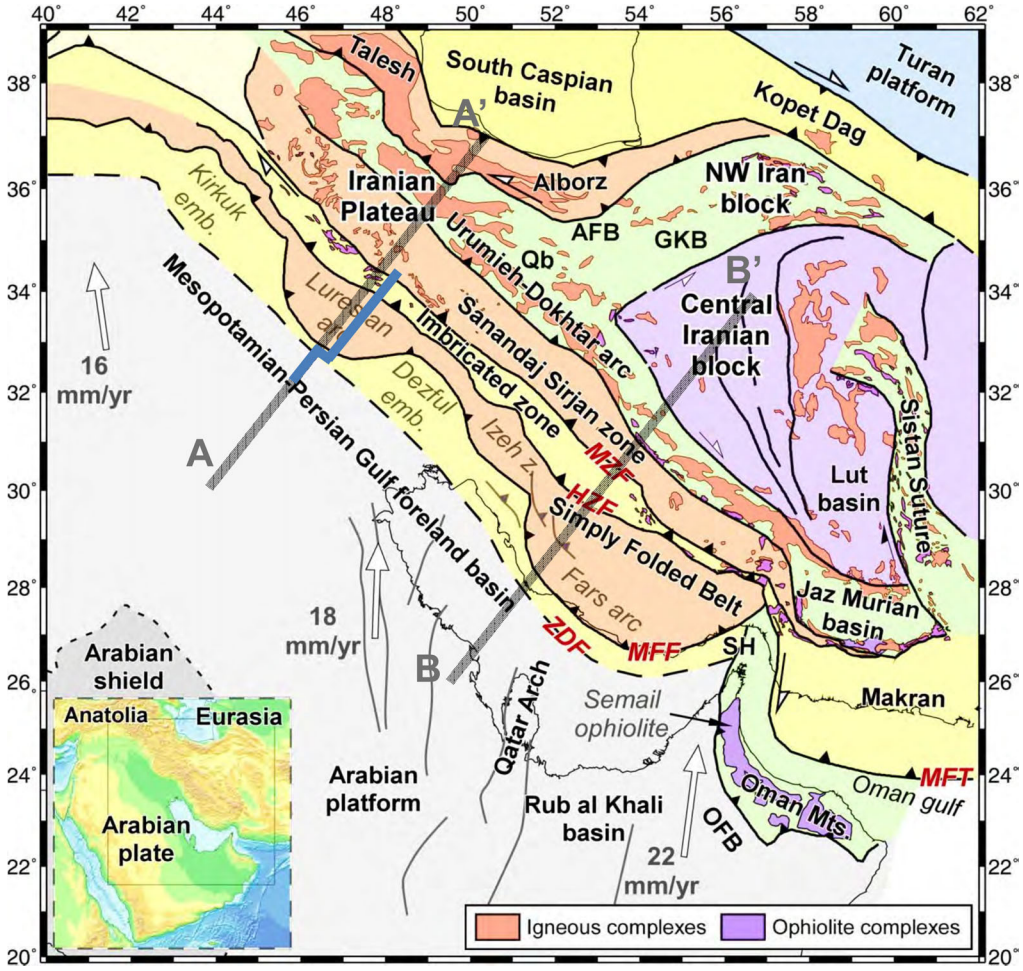

Figure 1. Structural map showing the main tectonic units of the Zagros Mountains and adjacent areas, and location of the selected profiles (thick grey lines) A–A′ and B–B′ (modified after Jiménez-Munt *et al.* 2012). The colours assigned to the different tectonic units are not related to age or lithology, but are used to highlight their limits. White arrows correspond to the relative plate velocities of the Arabian Plate with respect to a fixed Eurasian Plate. Thick blue line indicates the balanced geological cross-section by Vergés *et al.* (2011). ZDF, Zagros deformation front; MFF, main frontal fault; HZF, high Zagros fault; MZF, main Zagros fault; Qb, Qom basin; GKB, Great Kabir basin; and AFB, Alborz foredeep basin; OFB, Oman foreland basin; SH, Strait of Hormuz; MF, Minab fault; MFT, Makran frontal thrust.

(Molinaro *et al.* 2005; Motavalli-Anbaran *et al.* 2011) confirmed a pronounced lithospheric mantle thinning from the Arabian Plate to Central Iran along several lithospheric cross-sections. Jiménez-Munt *et al.* (2012) calculated the lithospheric structure of Iran with the aim of separating the regional/residual gravity anomalies. These authors used a 1-D approach combining geoid height and elevation data and considering the crust as a homogeneous layer with a constant average density and a temperature-dependent lithospheric mantle density. The authors also found that the Mesopotamian–Persian Gulf foreland basin is characterized by a thick lithosphere, which thins out drastically underneath the high Zagros and Central Iran.

A remarkable feature is that, all the previously referred lithospheric models in the region (e.g. Molinaro *et al.* 2005; Motavalli-Anbaran *et al.* 2011; Jiménez-Munt *et al.* 2012) are based on a 'pure' thermal approach, which considers that the density of the lithospheric mantle is only temperature dependent and equivalent to the density of the underlying asthenosphere, corrected by thermal expansion. Strong limitations of this approach are: (i) the lithospheric mantle is assumed to be homogeneous in composition, (ii) phase changes are not considered and (iii) the density of the asthenosphere is constant everywhere. A major restriction is that, the resulting lithospheric mantle structure cannot be directly compared with *Pn*-, *Sn*-, *P*- and *S*-wave velocities obtained from seismic experiments and tomographic models.

In contrast to previous studies, in this work, we apply a self-consistent petrological-geophysical approach (Afonso *et al.* 2008; Fullea *et al.* 2009), which integrates potential fields (gravity and geoid), isostasy (elevation), thermal equations (heat flow and temperature distribution) and mantle mineral physics. Hence, the calculated mantle density, thermal conductivity and elastic parameters (*Vp* and *Vs*) depend on temperature, pressure and chemical composition through the equations of state. This paper addresses for the first time, the relative contributions of temperature and composition on density and seismic velocities in the upper mantle beneath the Arabia-Eurasia continental collision region with the aim of (i) making compatible seismic and thermal model results, (ii) quantifying the effect of mineral physics on previous results from integrated thermal models and (iii) validating the lithospheric mantle thinning hypothesis. We present the crust and upper mantle structure down to 400 km depth along two transects across the Arabia–Eurasia collision from the Mesopotamian–Persian Gulf Foreland Basin (Arabian Foreland Basin) to Central Iran (Fig. 1), whose location was selected based on the availability of data and previous works.

2 GEOLOGICAL BACKGROUND AND TECTONIC SETTINGS

The Zagros orogen resulted from the long-lived NE-dipping subduction of the Neotethys Ocean, lasting from Late Cretaceous to Neogene, culminating with the continental collision between Arabia and Eurasia (e.g. Agard *et al.* 2011; Vergés *et al.* 2011; Mouthereau *et al.* 2012; McQuarrie & van Hinsbergen 2013). The Zagros mountain belt extends for more than 2000 km in a NW–SE direction, from eastern Turkey to the Hormuz Strait in southern Iran, where it connects to the Makran subduction zone (Fig. 1).

The Zagros orogenic system is composed of five structural domains, separated by significant thrust faults (Fig. 1). The Mesopotamian Foreland Basin along the Euphrates and Tigris Plain and its continuation in the Persian Gulf, formed by the flexure of the Arabian Plate in front of the Zagros fold-and-thrust belt (ZFTB). The fold-and-thrust belt (or simply folded belt) is separated from the foreland basin by the main frontal fault (MFF), creating a structural uplift of several kilometres, involving basement rocks and folding of the thick cover succession (e.g. Sepehr & Cosgrove 2004; Sherkati *et al.* 2006; Casciello *et al.* 2009; Emami *et al.* 2010). The imbricated zone (IZ), bounded by the high Zagros fault (HZF) to the southwest, is a highly deformed domain, involving multiple tectonic thrust sheets composed of sedimentary, radiolaritic and ophiolitic rocks, which represent the distal cover rocks of the Arabian Plate, as reconstructed in Vergés *et al.* (2011). The Sanandaj Sirjan zone (SSZ) is an Iranian continental block involving Palaeozoic to Cretaceous sedimentary and metamorphic rocks. This zone is thrusted to the SW, on top of the MZF. The Tertiary Urumieh Dokhtar Magmatic Arc (UDMA) formed on the Iranian crust in response to the northeastern subduction of the Neotethys Ocean and is thrusted to the NE above the Central Basin in Iran.

The Central Iran Basin (east Iran) is filled by a 6–8-km-thick Neogene sedimentary succession above Eocene volcanics and Cretaceous and Jurassic rocks (e.g. Morley *et al.* 2009). To the north, the Alborz Mountains were formed by the collision with Eurasia after the Palaeotethys Ocean subduction, which culminated in Triassic times (Berberian & King 1981; Sengör *et al.* 1988). The tectonic history is later characterized by a Late Cretaceous–Palaeocene thrusting event followed by Eocene backarc extension during early-middle and late Eocene (Allen *et al.* 2003; Fig. 1). The South Caspian Basin, at the northern edge of our A–A′ profile, represents the deepest basin in the world with more than 17-km-thick Oligocene-Recent sedimentary succession, mildly folded and thrusted as a result of the Arabian–Eurasia collision (e.g. Egan *et al.* 2009).

3 METHOD

The methodology used in this work is based on the *LitMod-2D* code (Afonso *et al.* 2008), which combines geophysical and petrological data, in order to study the crust and upper mantle structures from a thermal, compositional, seismological and density point of view. The code allows calculation of the 2-D distribution of temperature, density and mantle seismic velocities down to 400 km depth and the gravity and geoid anomalies, elevation and surface heat flow. A forward modelling scheme is applied by comparing the model outputs (elevation, gravity and geoid anomalies, surface heat flow and mantle seismic velocities) with observed data and modifying parameters and model geometry (crust and lithosphere) within the experimental uncertainties, until the best fit is obtained.

The model domain is composed of multiple polygons, representing the different crustal and mantle bodies, to which a triangular finite element mesh is adapted. Each crustal body is associated with a single lithology, described by a set of thermophysical parameters (density, thermal conductivity and volumetric heat production). Density and thermal conductivity can be pressure- and/or temperature-dependent, whereas, volumetric heat production can be either constant or exponentially decreasing with depth. The geometry and properties of the crustal bodies are assigned according to the geological structure and constrained by existing data.

The conductive heat transport equation is solved by using the finite element method in steady-state, with the following boundary conditions: 0 °C at the surface; 1330 °C at the lithosphere–asthenosphere boundary (LAB); and no heat flow across the lateral boundaries of the model. Beneath the LAB, the algorithm considers a 40-km-thick thermal buffer with a temperature of 1400 °C at its base, in order to avoid unrealistic discontinuities between the conductive thermal gradient within the lithospheric mantle and the adiabatic thermal gradient within the asthenosphere. The temperature gradient between the thermal buffer and the base of the model is restricted to $0.35 < dT/dz < 0.50$ °C km^{-1}, otherwise the temperature at 400 km depth, initially set to 1520 °C, is modified accordingly (see Afonso *et al.* 2008 for further details).

Stable mineral phases and assemblages were calculated from the bulk composition expressed in the NCFMAS system (Na_2O–CaO–FeO–MgO–Al_2O_3–SiO_2) and pressure and temperature conditions were calculated using a Gibbs free-energy minimization algorithm (details in Connolly 2005). In this work, we used a modified version of the Holland & Powell (1998) thermodynamic database (Afonso & Zlotnik 2011). The resulting thermodynamic tables are generated by Perple-X (Connolly 2005), describing densities, elastic and thermophysical parameters of the end-member minerals. The asthenosphere was considered to be compositionally homogeneous, due to its convective nature, whereas, the lithospheric mantle can show lateral compositional variations, depending on the geodynamic context of a certain region.

Gravity and geoid calculations were performed by using simple algorithms applied to the elements of the mesh and absolute elevation was calculated for each column, under the assumption of local isostasy (Zeyen & Fernàndez 1994; Zeyen *et al.* 2005). Seismic wave velocities were calculated from thermodynamics and equations of state as a function of composition, pressure and temperature. Anelastic effects were computed as a function of the grain size, oscillation period, P–T conditions and empirical parameters (Afonso *et al.* 2008 and references, therein).

4 DATA

The modelling approach used in this study was constrained by four different types of data: (1) Elevation, surface heat flow, and potential field data collected from global databases. (2) Crustal structure and Moho depths derived from geological cross-sections and waveform inversion, receiver functions, and receiver functions coupled with surface wave analysis. (3) LAB geometry inferred from numerical models, seismic tomography models and, partly, from receiver functions. Since Moho and LAB depths contain intrinsic uncertainties depending on the experimental and modelling approaches, they were used to construct the initial lithospheric structure model and were then further modified within the uncertainties range. (4) Mantle seismic velocities inferred from seismic tomography models (global and regional) and from some seismic profiles. Due to the lack of xenolith suites in the study area, we estimated the composition of the lithospheric mantle, according to the crustal tectonothermal age

of the different domains, following global studies (e.g. Griffin *et al.* 2003, 2009; O'Reilly & Griffin 2006).

4.1 Global data sets

Gravity data (Fig. 2a) for Iran came from Getech 10 km × 10 km grid data (http://www.getech.com), while in the rest of the region, the Bouguer anomaly was computed by applying the complete Bouguer correction to satellite free-air data (Sandwell & Smith 1997) using the FA2BOUG code (Fullea *et al.* 2008) with a reduction density of 2670 kg m^{-3}. Geoid height data were derived from the Earth Geopotential Model EGM2008 (Pavlis *et al.* 2008) with spatial resolution of 5 min-arc. Long wavelengths (>4000 km) have been removed by subtracting spherical harmonics up to degree and order 9 (>400 km). The obtained geoid anomaly is shown in Fig. 2(b) with maximum amplitude of ∼30 m over a distance of 500 km between the Persian Gulf and SE-Zagros.

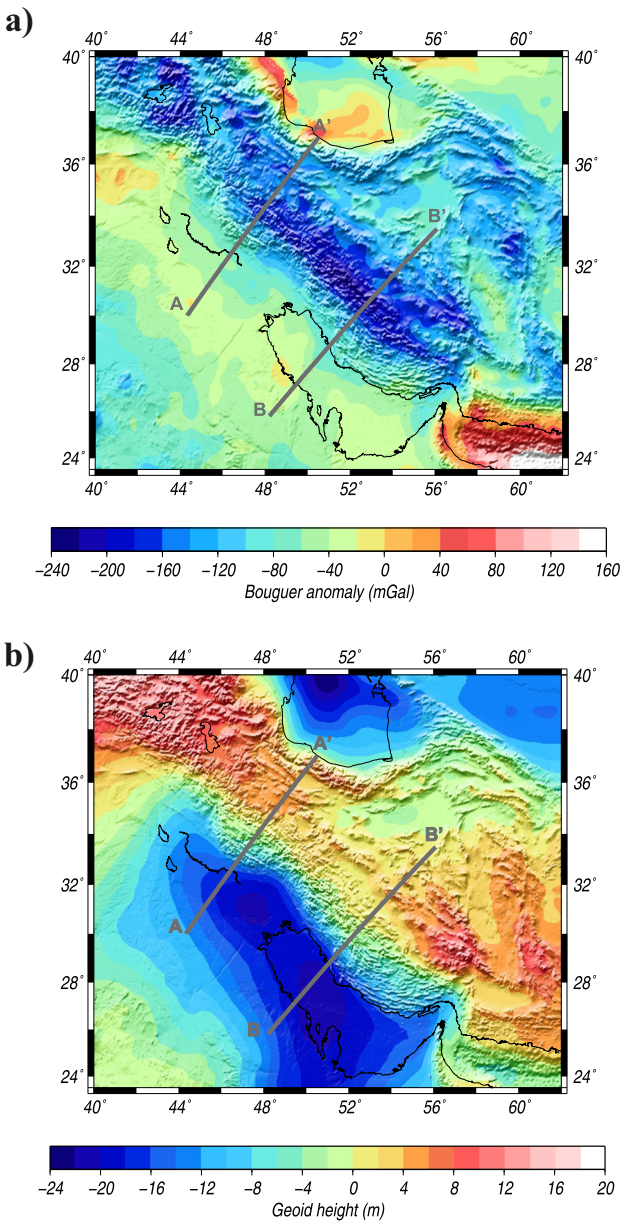

Figure 2. Potential fields in the study area. (a) Bouguer anomaly from Getech data in Iran and calculated from satellite free-air anomaly in the rest of the region (see text for details). (b) Geoid height from EGM2008 model. Spherical harmonics up to degree and order 9 have been removed. Shading indicates elevation.

Elevation data (Fig. 3) come from 1×1 min-arc resolution ETOPO1 (Amante & Eakins 2009) global elevation model http://www.ngdc.noaa.gov/. The Arabian Platform and the foreland basin show a smooth topography with a minimum in the Persian Gulf, whereas in the Zagros Mountains the elevation increases rapidly from sea level to 1500 m in the ZFTB, achieving an average of 3000 m of altitude in the Imbricate Zone and in the Alborz.

Surface heat flow measurements, although being particularly abundant in Red Sea, Gulf of Aden, Anatolia and Caspian Sea, are very scarce in Iran and the Arabian Platform (e.g. Pollack *et al.* 1993; Förster *et al.* 2007; Lucazeau *et al.* 2010; Rolandone *et al.* 2013). A total of three heat flow sites were available in the study region located over 100 km far from the selected profiles and therefore, thus we are not considering surface heat flow as a constraint in our modelling.

4.2 Crustal structure and depth to Moho

Fig. 3 shows a compilation of obtained Moho depth values inferred from seismic studies, using receiver functions and surface wave dispersion analysis. Crustal thickness varies from 35 to 45 km in the Mesopotamian Foreland and Arabian Platform, to between 44 and 69 km below the Zagros Mountains with the maximum values beneath the SSZ zone (Paul *et al.* 2006, 2010; Gök *et al.* 2008; Gritto *et al.* 2008; Nasrabadi *et al.* 2008; Manaman *et al.* 2011). A crustal root is identified below the Alborz (Nasrabadi *et al.* 2008; Sodoudi *et al.* 2009; Paul *et al.* 2010; Radjaee *et al.* 2010), with the crust–mantle boundary in a depth of 53–67 km. See also Jiménez-Munt *et al.* (2012) for a thorough compilation of crustal thickness data.

The geological structure of the Zagros Mountains is outlined by different studies (e.g. McQuarrie 2004; Mouthereau *et al.* 2007; Casciello *et al.* 2009; Emami *et al.* 2010; Vergés *et al.* 2011), detailing the stratigraphy of the ZFTB and showing evidences for the compressive deformation affecting both the sedimentary cover and basement. We also used geological cross-sections, available from the geological maps by the National Iranian Oil Company (NIOC) to construct the shallower part of the profiles (7–10 km depth).

Our A–A′ profile runs parallel to the geological cross-section in Vergés *et al.* (2011) and continues northwards, approximately following the northern seismic profile (Zagros03) by Paul *et al.* (2010), and southwards through the Mesopotamian Foreland Basin. Profile B–B′ coincides with the southern transect (Zagros01) by Paul *et al.* (2006, 2010), and extends southwestwards crossing the Persian Gulf (Figs 1 and 3) until it reaches the Arabian Platform.

4.3 Depth to the LAB

The LAB depth of the Arabia–Eurasia collision zone has been investigated by using numerical models integrating different geophysical data (Molinaro *et al.* 2005; Motavalli-Anbaran *et al.* 2011; Jiménez-Munt *et al.* 2012), and by using seismic techniques (Hansen *et al.* 2007; Mohammadi *et al.* 2013). Molinaro *et al.* (2005) show a profile crossing perpendicularly to the southern Zagros (Fig. 3) and propose a sharp lithospheric thinning below the range. Their results show that the LAB shallows from ∼220 km beneath the Persian Gulf to ∼100 km beneath the ZFTB, and it deepens again northeastwards

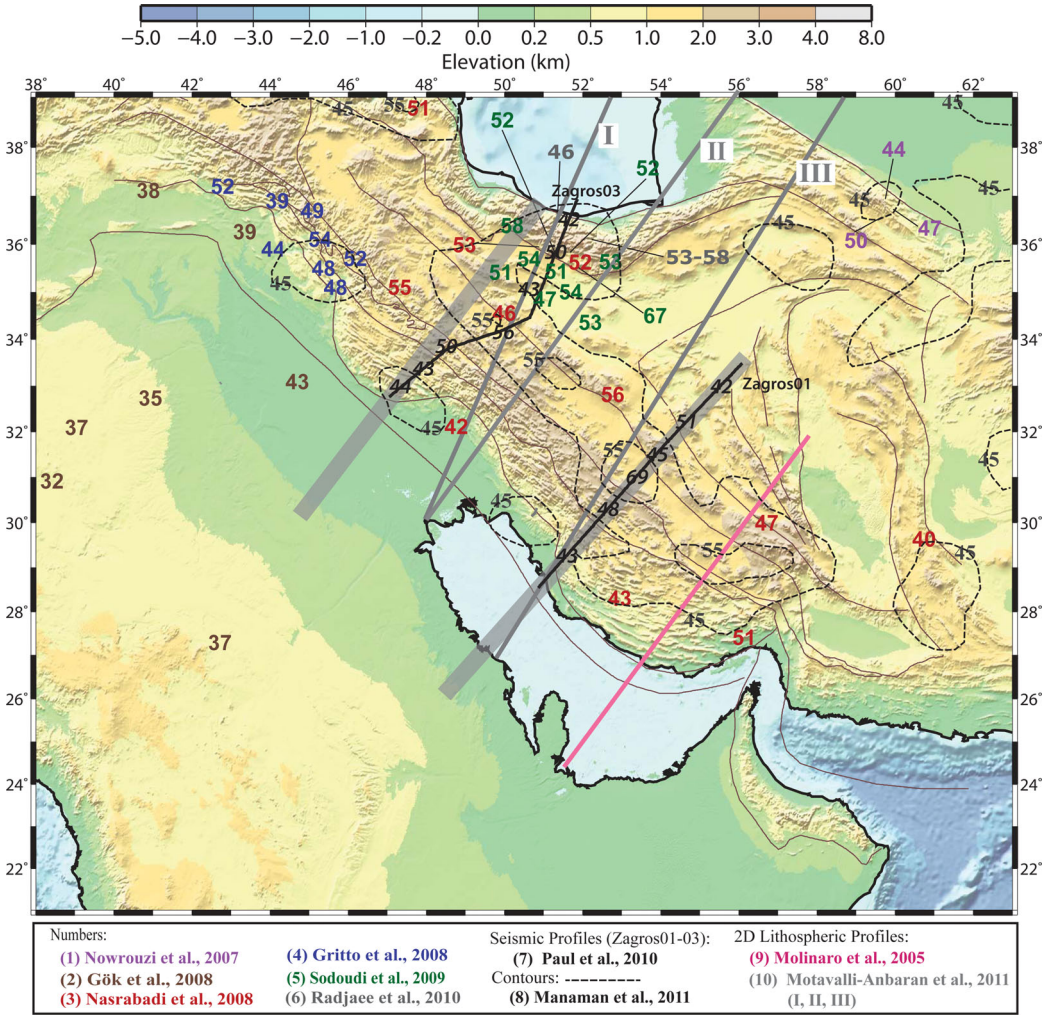

Figure 3. Topography map of the study area, crustal thickness values (numbers) and localization of 2-D lithospheric modelling profiles (heavy continuous lines, grey and pink) from other studies (modified after Jiménez-Munt *et al.* 2012). Black dashed contours are the results from regional tomographic models (Manaman *et al.* 2011). Grey wide lines denote the localization of A–A′ and B–B′ profiles of this study. Grey thin lines correspond to the main structural boundaries (see Fig. 1).

to depths of 140 km in Central Iran. Motavalli-Anbaran *et al.* (2011) present three SW–NE transects crossing Iran from the Arabian Platform to the South Caspian Basin and the Turan Platform. The results suggest that the lithospheric thinning (LAB depths of 100–120 km) affects the northern Zagros Mountains extending to Central Iran. Jiménez-Munt *et al.* (2012) show a thick lithosphere beneath the Persian Gulf and the ZFTB (180–220 km) thinning underneath the SSZ and Central Iran (160–140 km).

Results from receiver function studies reveal trends similar to the numerical models, but a consistently shallower LAB. Mohammadi *et al.* (2013) image the LAB at ∼130 km depth beneath the ZFTB, ∼150 km beneath the SSZ and 80–85 km in Central Iran. In the Arabian Platform, Hansen *et al.* (2007) propose the base of the lithosphere as lying at ∼160 km depth in the Arabian Shield-Platform boundary (∼45° East Lon), shallowing northeastwards to ∼135 km depth.

4.4 Mantle seismic velocities

Fig. 4 shows the *Vp* anomaly distribution along the selected profiles, resulting from a global tomography model based on *P*-wave arrival times. The global *P*-wave velocity model shown here has been obtained using the same method described in Bijwaard *et al.* (1998), incorporating additional earthquakes from 1995 to 2002 and arrival times (Villaseñor *et al.* 2003). In total, more than 14 million arrival times from 300 000 earthquakes were reprocessed using the EHB methodology (Engdahl *et al.* 1998). The ray paths corresponding to these new arrival times sample, mainly, the uppermost mantle with a resolution of 0.5° × 0.5° in area and 25–50 km in depth. Along the A–A′ transect, a 50° NE-dipping boundary is interpreted as the Arabia–Eurasia boundary lying along the MZF. High velocity perturbations (>1%) are imaged, extending from the Arabian Platform to the MZF, reaching the ∼200 km depth. A slab feature is dipping towards the NE beneath the SSZ. Along the B–B′ transect, the maximum of the high velocity feature is localized beneath the Arabian Platform and the Persian Gulf, until ∼230 km depth. The lateral transition to the low velocity anomaly of the Central Iran is less abrupt than along the A–A′ profile. Slight lateral velocity variations (±0.2%) characterize the lithospheric mantle beneath the Zagros Mountains, and small features with inverse velocity can be observed in the shallower mantle below the MFF discontinuity (low velocity anomaly down to 50 km of depth) and below the IZ (high velocity at 50–100 km depth).

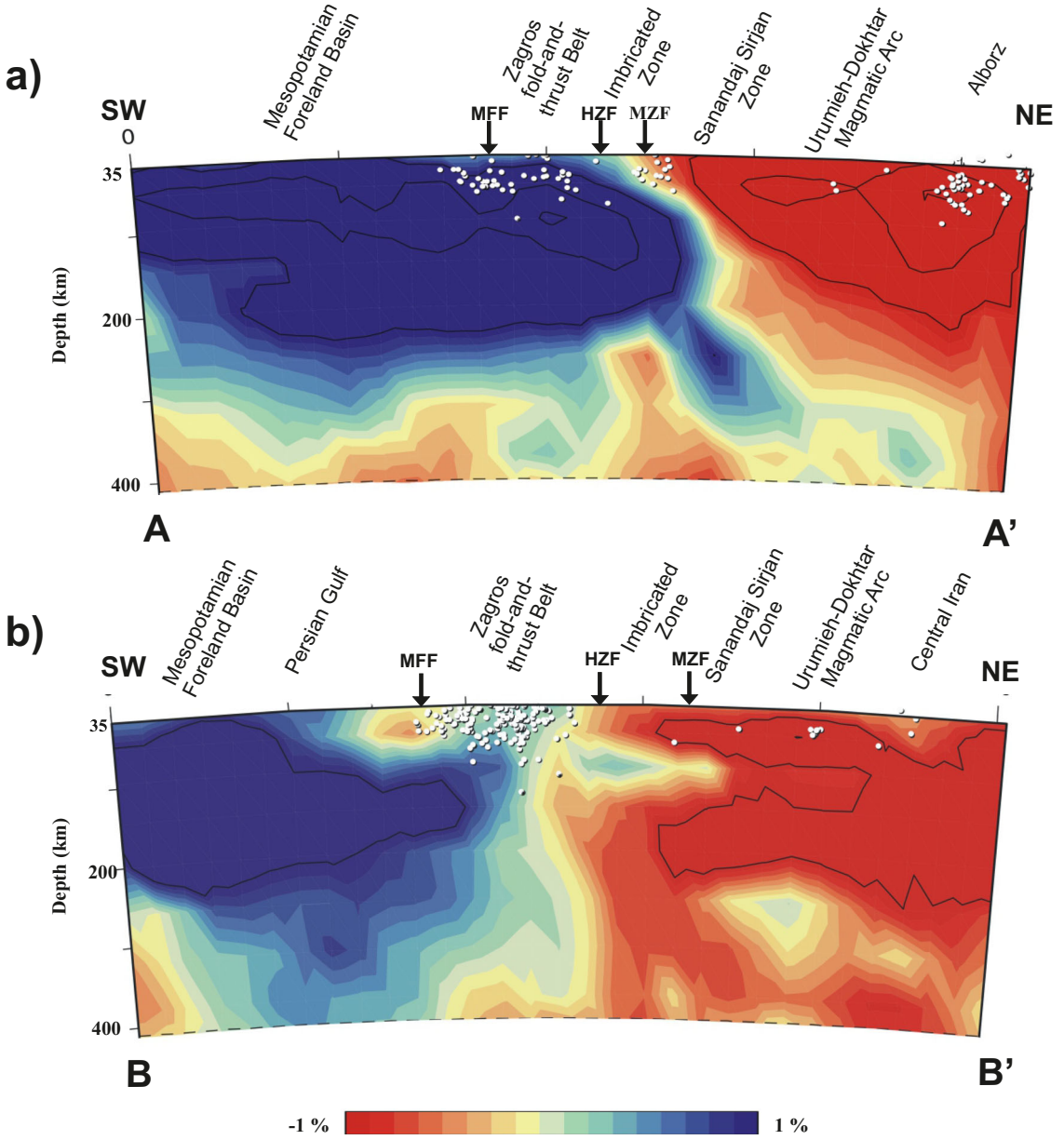

Figure 4. P-wave tomography along A–A′ (a) and B–B′ (b) profiles from 35 to 400 km depth. Global reference model used—AK135 (Kennett *et al.* 1995). HZF, high Zagros fault; MFF, main frontal fault; MZF, main Zagros fault.

The sharp change in seismic velocities in the Arabia–Eurasia collision zone is also observed in other published tomography profiles (Ritzwoller *et al.* 2002; Maggi & Priestley 2005; Kaviani *et al.* 2007; Manaman & Shomali 2010). The Arabian lithosphere is, overall, characterized by high seismic velocity, while the Iranian lithosphere is markedly slower. The transition between the two velocity domains is located, approximately, beneath the MZF. However, it is still unclear whether low velocities characterize only the lithospheric mantle beneath Central Iran or also the lithospheric mantle beneath the inner parts of the Zagros Mountains (UDMA and SSZ). Manaman & Shomali (2010) observed low velocities below the Urumieh Dokhtar Magmatic Arc, whereas, Maggi & Priestley (2005) only observed them below Central Iran. Alinaghi *et al.* (2007) observed a change in the low velocities across the strike of the Zagros Mountains, with the high velocities of Arabia penetrating more into Iran in the NW Zagros than in the central Zagros (nearby our B–B′ profile). Kaviani *et al.* (2007) found high *S*-wave velocities beneath the Zagros Mountains, and low *S*-wave velocities in the shallow mantle below the SSZ and UDMA regions. According to the authors, the 0.5 km s^{-1} difference of *Vs* is, likely, due to a compositional change associated with high temperatures beneath the Sanandaj Sirjan and Urumieh Dokhtar Magmatic Arc. Simmons *et al.* (2011), using a multi-event location approach and 3-D ray tracing, imaged a fast-velocity anomaly beneath the Arabian Platform extending several kilometres beneath Iran at a depth of ~150 km, which is interpreted as the underthrusting of the Arabian lithosphere beneath Central Iran.

4.5 Lithospheric mantle composition

Global data from mantle-derived xenoliths and garnet xenocrystals in volcanic rocks and exposed massifs document a secular

Table 1 Chemical compositions used in the models for mantle bodies (see Figs 7 and 8).

Mantle compositions in the NCFMAS system (%)				
	Mantle 1 Pr3 Proterozoic (Griffin *et al.* 2009)	Mantle 2 Pr6 Proterozoic (Griffin *et al.* 2009)	Mantle 3 Pr3-Tc3[a]	Asthenosphere–PUM Primitive upper mantle (McDonough & Sun 1995)
SiO_2	45.2	45.4	45	45
Al_2O_3	2	3.7	3	4.5
FeO	7.9	8.3	7.9	8.1
MgO	41.6	39.9	42	37.8
CaO	1.9	3.2	1.9	3.6
Na_2O	0.13	0.26	0.13	0.25
Total	98.73	100.76	99.93	99.25

[a]Intermediate composition between Pr3 (Proterozoic) and Tc3 (Phanerozoic) from Griffin *et al.* (2009).

compositional evolution of the lithospheric mantle through time, revealing a depletion in Fe, Ca and Al contents from Archean to Phanerozoic times (Poudjom-Djomani *et al.* 2001; Griffin *et al.* 2003, 2009; O'Reilly & Griffin 2006). Depletion in incompatible elements, in particular Fe, has important consequences for geophysical properties, since it results in lower densities and higher seismic velocities (Poudjom-Djomani *et al.* 2001; Artemieva 2006). In this work, we assume that the formation (or modification) of crust and mantle are broadly contemporaneous and, hence, we refer to the tectonothermal age of the crust in order to constrain the composition of the lithospheric mantle.

The age of the Iranian lithosphere is <50 Ma, whereas, available geochronological data indicate a Neo-Proterozoic age (540–850 Ma) for the Arabian Platform (Artemieva 2006; Stern & Johnson 2010). Therefore, we consider Proterozoic compositions for the lithospheric mantle beneath the Arabian Foreland Basin and a more fertile Phanerozoic composition for the lithospheric mantle below the Zagros Mountains. Due to the lack of mantle-derived xenoliths in the study region, we adopted standard NCFMAS compositions from Griffin *et al.* (2009) for the lithospheric mantle bodies. The chosen compositions provide the best fit of seismic velocities and densities (elevation). This is the reason for considering two Proterozoic mantles in the Arabian Plate. The asthenosphere is considered to have a primitive upper mantle (PUM) composition (McDonough & Sun 1995). In order to smooth the compositional change between the lithospheric mantle and the underlying asthenosphere, we introduced a layer of 10–20 km thickness with an intermediate composition between the asthenosphere and the corresponding lithospheric mantle above. Table 1 summarizes the mantle compositions considered in this study.

Fig. 5 illustrates how lithospheric mantle composition affects the resulting density and seismic velocities in a 210-km-thick lithosphere with a 42-km-thick crust, which is a representative structure of the Arabian Plate. All compositions show a density increase of between 10 kg m^{-3} for Mantle 1 and 25 kg m^{-3} for PUM around 50 km depth, related to the spinel-garnet phase transition. The spinel-garnet transition marks also an increase in *P*-wave velocities of between 0.05 km s^{-1} for Mantle 1 and 0.08 km s^{-1} for PUM, and an increase in *S*-wave velocities of 0.01–0.02 km s^{-1}. Down to this phase transition, the density and seismic velocity depth variations are very similar for all compositions, increasing with depth for density and *P* waves and decreasing for the *S* waves, until the LAB. The lighter composition corresponds to Mantle 1, which is ∼12 kg m^{-3} less dense than Mantle 3, ∼27 kg m^{-3} less dense than Mantle 2, and ∼37 kg m^{-3} less dense than PUM. Note that the density–depth evolution within the lithospheric mantle depends on the competing effects of temperature and pressure and, therefore, on the lithospheric structure. The depleted Mantle 1 is also markedly slow with respect to the other composition types, particularly, for the *P*-wave velocities, which indicate that it is ∼0.04 km s^{-1} slower than Mantle 2 and 0.05 km s^{-1} slower than the fertile PUM.

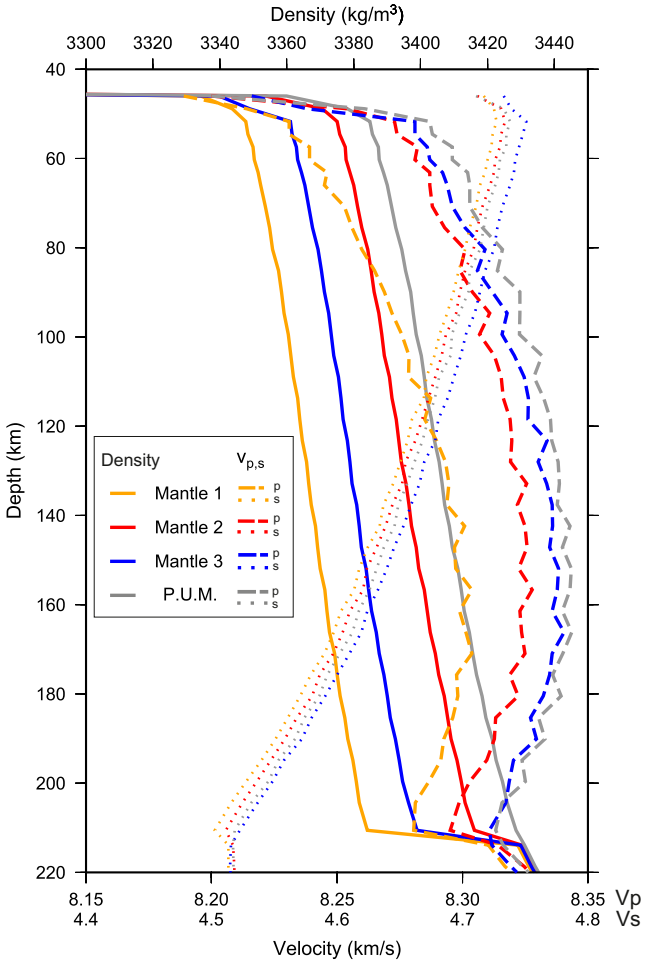

Figure 5. Density and velocity variations with depth for each mantle composition, considering a flat model with parallel layers, Moho discontinuity at 42 km depth and LAB at 210 km depth. Mantle compositions refer to Table 1.

5 RESULTS

The forward modelling scheme required an initial model including the geometries of the crustal and lithospheric mantle bodies and

their physical parameters. As a general procedure, we kept the initial crustal model (geometry and physical parameters) and we only modified it when strictly necessary, in order to fit the high frequency components of topography and gravity signals, after trying different mantle compositions and mantle bodies' geometries. Crustal modifications are always within the uncertainties associated with experimental data. The final lithosphere geometry, as well as chemical composition and physical parameters are assigned in order to obtain the best fit with all the observables (gravity, geoid, elevation, mantle seismic velocities and derived tomography models).

5.1 Crustal structure

The resulting best fit crustal models for the selected A–A′ and B–B′ profiles are shown in Fig. 6. The different lithologies are characterized by the physical parameters detailed in Table 2. In the sedimentary cover, we distinguished Tertiary, Mesozoic and Palaeozoic sediments. The SSZ and the Urumieh Dokhtar Magmatic Arc are characterized by granitic and metamorphic complexes, differently distributed along the two profiles. The crystalline basement is represented by the upper-middle crust and the lower crust. Along the A–A′ profile each of these layers is ∼15 km thick in the Arabian Platform and foreland basin, and they vary their relative thicknesses towards the NE. Along B–B′ profile, the lower crust is considerably thicker than the upper-middle crust from the foreland basin to Central Iran, particularly, in the SSZ where the crust–mantle boundary reaches 63 km depth. In order to reconcile gravity, geoid and elevation data with the crustal thickness inferred from receiver functions (Paul *et al.* 2006, 2010), we included a high density lower-crustal body at depths of ≥50 km, with a density of 3500 kg m^{-3}. This body would correspond to a 100% eclogitized lower crust, characterized by relatively low velocity and high density. Alternatively, we can also consider a ∼10 km shallower Moho which would require a slight modification of the upper and middle crustal bodies in this region.

5.2 Lithospheric mantle structure

The best fit models along the selected profiles are illustrated in Figs 7–10, with the crustal structures described previously and shown in Fig. 6. The data adjustment for both profiles are shown in Table 3. The root mean square error (RMSE) between observed and calculated data has been determined according to

$$\mathrm{RMSE} = \frac{\left[\sum_{i=1}^{N} \left(x_{(i)\mathrm{obs}} - x_{(i)\mathrm{calc}}\right)^2\right]^{\frac{1}{2}}}{N} \quad (1)$$

with x_{obs} and x_{calc} being the observed and calculated data, respectively, and N is the total number of points along the profile.

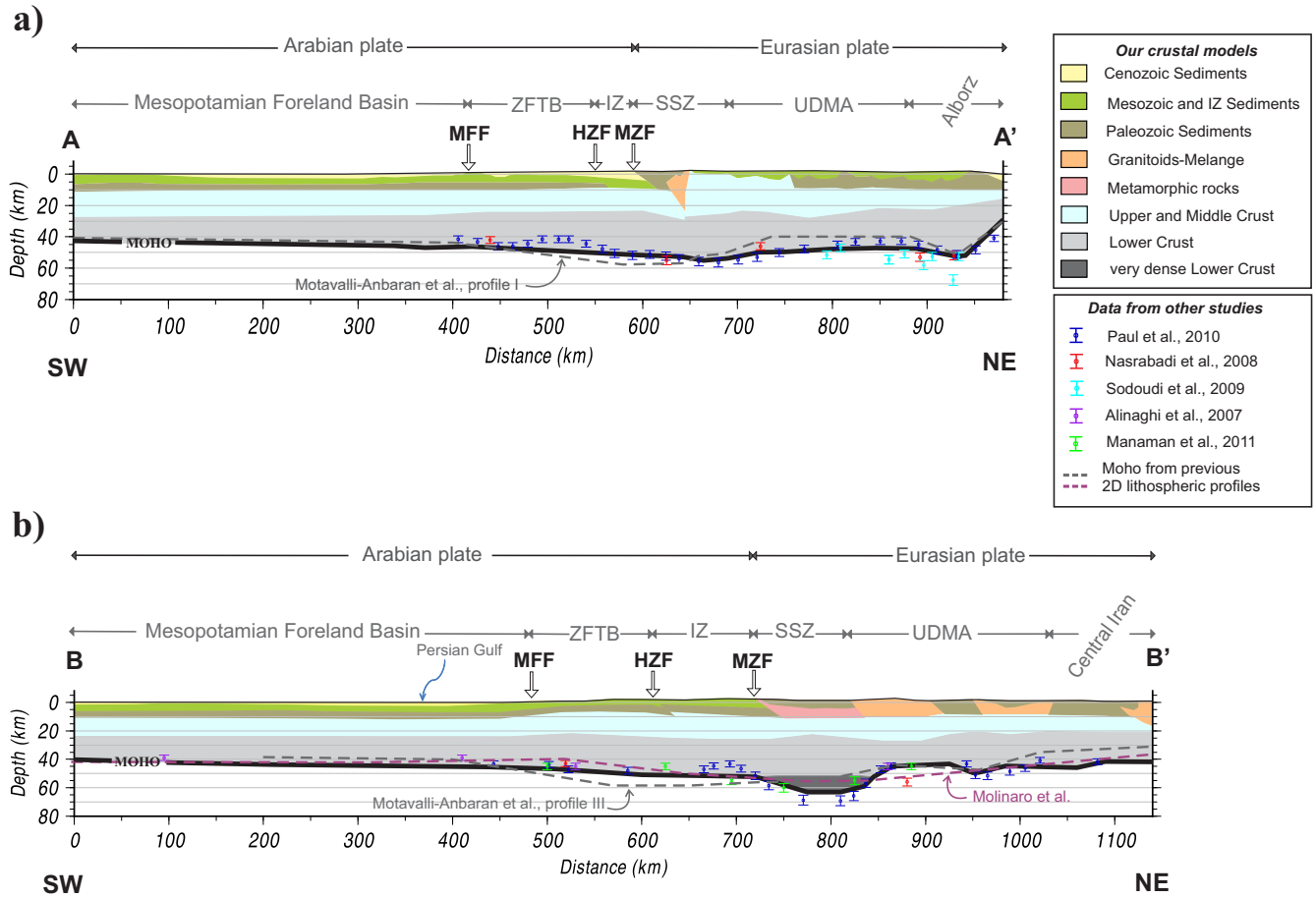

Figure 6. Crustal model for A–A′ (a) and B–B′ profile (b). Dashed lines indicate the Moho discontinuity from published 2-D lithospheric profiles (Molinaro *et al.* 2005; Motavalli-Anbaran *et al.* 2011). Physical properties of crustal bodies are reported in Table 2. HZF, high Zagros fault; IZ, imbricated zone; MFF, main frontal fault; MZF, main Zagros fault; SSZ, Sanandaj Sirjan zone; UDMA, Urumieh Dokhtar Magmatic Arc; ZFTB, Zagros fold-and-thrust belt.

Table 2 Physical properties of the materials used in the modelling: depth-varying density, ρ (kg m^{-3}); thermal conductivity, K [W (Km)$^{-1}$]; volumetric heat production, H (μW m^{-3}). The heat production in the lithospheric mantle and asthenosphere is 0.02 μW m^{-3}.

Material description	Density, ρ (kg m^{-3})	Thermal conductivity, K [W (Km)$^{-1}$]	Heat production rate H (μW m^{-3})
Cenozoic sediments	2450–2580	2.0	1.0
Mesozoic and imbricated zone sediments	2650	2.0–2.5	1.0
Paleozoic sediments	2700	2.5	1.0
Granitoids - Melange	2730–2780	2.0–3.1	1.0–2.0
Metamorphic rocks	2850	2.0	0.5
Upper crust	2820–2840	3.0	1.0
Lower crust	2980–2995	2.2	0.4
High dense lower crust	3500	2.0	0.25

5.2.1 Mantle chemical composition

In order to fit the observables (gravity, elevation, geoid and seismic velocities), we considered three different lithospheric mantle compositions (Mantles 1, 2 and 3 in Table 1). The overall composition of the lithospheric mantle along both profiles falls into the lherzolitic field. However, slight changes in the bulk composition (0.2–2.1 wt% variation) have been considered along both transects according to the age-composition variations. The composition of the deep lithospheric mantle portion of the southwestern Arabian Platform with Mg# ∼90.4 (Mantle 1 in Table 1), changes progressively towards the Mesopotamian Foreland Basin to a mantle type richer in FeO, Al_2O_3 and CaO with Mg# ∼90.6 (Mantle 2 in Table 1). This composition is also assumed to be predominant in the accreted terrains of the Eurasian Plate, including the Urumieh Dokhtar Magmatic Arc, Alborz and the Central Iran. In the region below the ZFTB and the IZ the composition is depleted in FeO, Al_2O_3, CaO and enriched in MgO (Mantle 3 in Table 1), resulting in a less dense lithospheric mantle. This depleted composition extends, partly, beneath the SSZ in profile A–A′ and until the UDMA in profile B–B′. Although falling into the lherzolitic field, Mantle 3 composition shows similarities with respect to the harzburgite-type composition, observed in the ophiolitic complexes outcropping in the Imbricated and SSZs, the depletion being related to intense mantle melt extraction during subduction (Shervais 2001; Ghasemi & Talbot 2006; and references, therein). The mantle mineral assemblages vary according to the P–T conditions and to the main oxides composition. Olivine is, obviously, abundant everywhere (61–65 wt%), especially in its Mg-rich phase (48–49 wt%); the 22–30 wt% of the rocks is formed by pyroxenes and the residual 8–15 wt% by garnet, present already at shallow depths. Garnet phase increases with depth, although, depleted in Fe, Al and Ca elements. Mantle 3 is characterized by a lower content in garnet and pyroxene with respect to Mantle 2 and Mantle 1, especially at shallower levels, due to the depletion in Al_2O_3 and CaO. The proposed enrichment in Al_2O_3 and CaO towards Central Iran is in agreement with a recent geochemical study on xenolith samples from NE Iran (Su *et al.* 2014).

5.2.2 Geometry and temperature–density distributions

A significant variation of the lithospheric mantle thickness is the most striking feature of the model outputs along both profiles (Figs 7 and 8). The LAB is located at ∼220 km depth below the Mesopotamian Foreland Basin, rising up to ∼125 km depth below the SSZ and the Urumieh Dokhtar Magmatic Arc and further NE towards the Alborz Mountains in profile A–A′ (Fig. 7), and towards Central Iran in profile B–B' (Fig. 8). The main difference between both profiles is that in A–A′ the thinning occurs over a very narrow region (<100 km width) starting in the contact between the IZ and the SSZ (the MZF). In contrast, in profile B–B′ lithospheric thinning occurs in the ZFTB (immediately north of the MFF) and extends northeastwards over a 300-km-wide region to the SSZ and the UDMA.

Temperature distributions are also similar in both profiles. The Arabian Foreland Basin is characterized by horizontal isotherms with moderate temperatures within the lithospheric mantle, with a Moho temperature of about 550 °C. The lithospheric mantle thinning affecting the SSZ, UDMA, Alborz and Central Iran deflects the isotherms upwards, especially near the LAB. Along profile A–A′, the Moho temperature beneath the Zagros Mountains increases from 650° below the ZFTB and IZ to 750–800 °C below the SSZ, and it continues, without significant variations, northwards towards the Alborz Mountains (Fig. 7). Along profile B–B′, the calculated Moho temperature increases from 600 °C in the ZFTB to 800 °C in the IZ, reaching a maximum of ∼900 °C in the SSZ, where the crust is thicker. In the UDMA and Central Iran, the Moho temperature is in the range of 650–700 °C.

The density distribution within the lithospheric mantle depends on composition and P–T conditions. Along profile A–A′ (Fig. 7), low densities (∼3310 kg m^{-3}) are found beneath the UDMA and the SSZ, increasing to the SW beneath the IZ and the ZFTB, related to the sharp lithospheric thickening, even though the mantle composition is lighter. Maximum densities (∼3430 kg m^{-3}) are found in the Arabian Plate due to both composition and mantle thickening. Along profile B–B′ (Fig. 8), the pattern of lateral density variations differs from profile A–A′ and the lower densities are found beneath the SSZ and the IZ, due to the combined effects of high temperature associated with lithospheric thinning and thick crust, and chemical composition. As in profile A–A′, the maximum densities correspond to the Arabian Plate, with similar values.

5.2.3 Seismic velocity distribution (Vp and Vs)

Fig. 9 shows the calculated seismic velocity (panels a, c) and seismic velocity anomaly distribution (panels b, d) for both *P*- and *S*-waves along profile A–A′. The velocity anomalies are calculated, with respect to the AK135 reference model (Kennett *et al.* 1995). Velocity variations related to compositional changes are smaller than those related to temperature and lithospheric thickness variations. *P*-wave velocities increase with depth within the lithospheric mantle and down to 400 km depth, whereas, *S*-wave velocities decrease with depth until the LAB and then increase again to the bottom of the model. The most remarkable feature is the sharp lateral change,

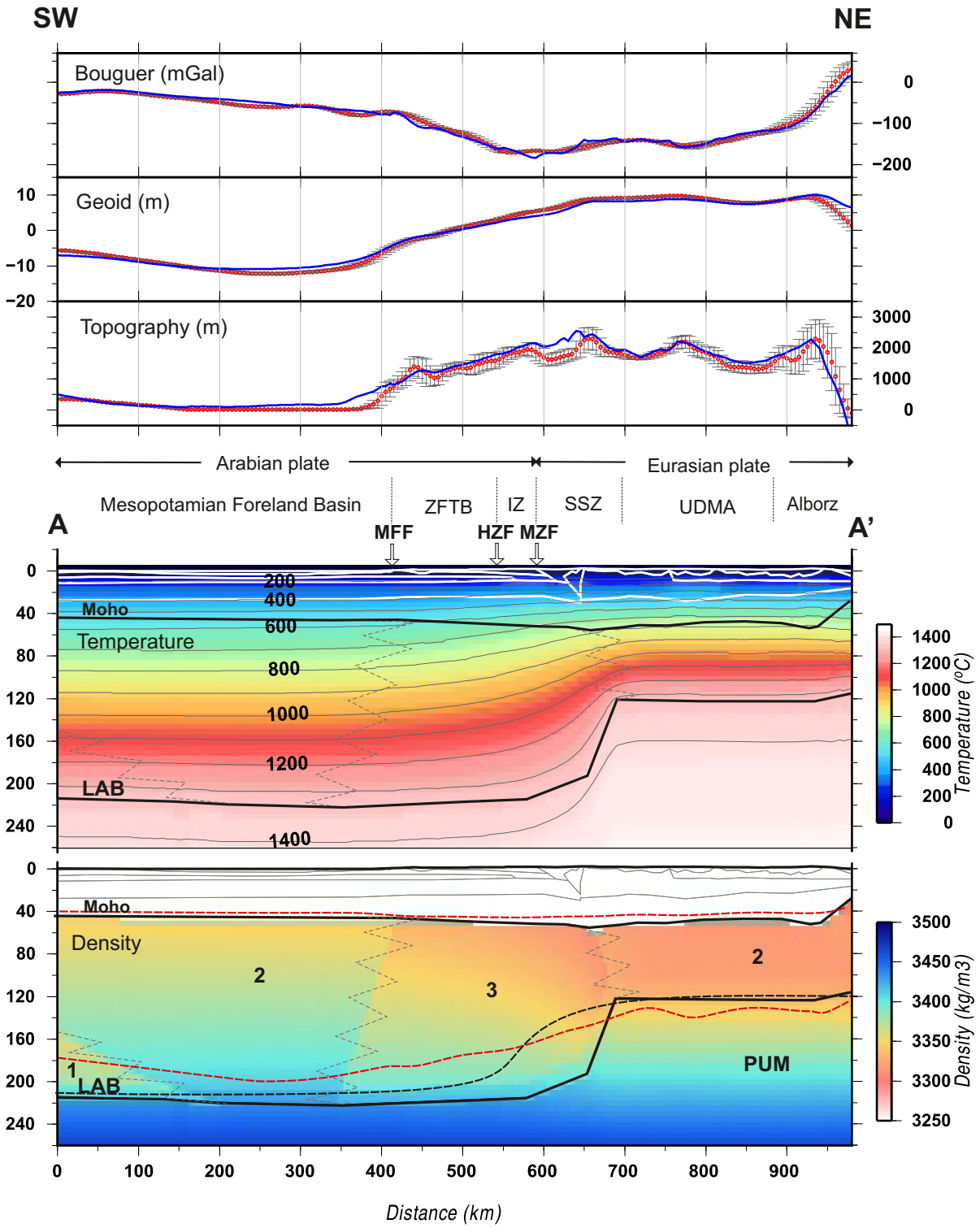

Figure 7. Modelling results for A–A′ profile. Red dots denote measured values and vertical dispersion bars with the standard deviation calculated on a strip of 50 km. Continuous blue lines represent the calculated values from the model. Dashed grey lines represent the transition between different chemical compositions or mantle domains. Numbers indicate different mantle composition (Table 1). Discontinuous lines indicate Moho and/or LAB depth geometry from by Motavalli-Anbaran *et al.* (2011) (profile I, black) and Jiménez-Munt *et al.* (2012) (red). HZF, high Zagros fault; IZ, imbricated zone; MFF, main frontal fault; MZF, main Zagros fault; SSZ, Sanandaj Sirjan zone; UDMA, Urumieh Dokhtar Magmatic Arc; ZFTB, Zagros fold-and-thrust belt.

observed in both *P*- and *S*-wave velocities, coinciding with the pronounced lithospheric thinning close to the plate suture. A low velocity anomaly characterizes the regions with a thin lithosphere, where, *Vp* in the lithospheric mantle decreases from 8.10 km s^{-1}, at 60 km depth, to 7.95 km s^{-1} at the LAB and *Vs* decreases from 4.60 to 4.35 km s^{-1}. In the Arabian Plate, the lithospheric mantle velocities are, generally, higher ranging from 8.15 to 8.33 km s^{-1} for *P* waves and from 4.50 to 4.68 km s^{-1} for *S* waves. A similar trend

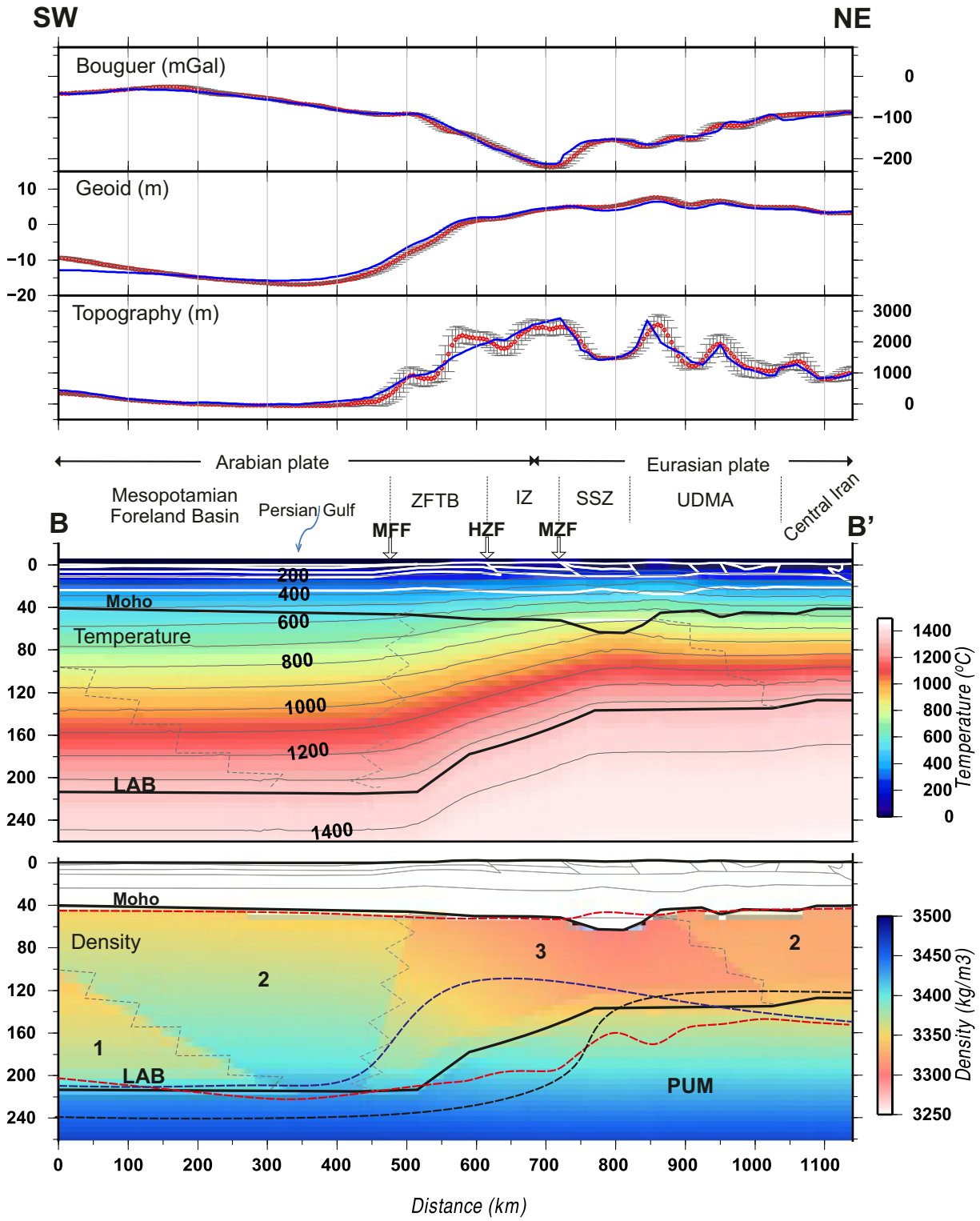

Figure 8. Modelling results for B–B′ profile. Red dots denote measured values and vertical dispersion bars with the standard deviation calculated on a strip of 50 km. Continuous blue lines represent the calculated values from the model. Dashed grey lines represent the transition between different chemical compositions or mantle domains. Numbers indicate different mantle composition (Table 1). Discontinuous lines indicate Moho and/or LAB geometry by Molinaro *et al.* (2005) (purple–blue), Motavalli-Anbaran *et al.* (2011) (profile III, black) and Jiménez-Munt *et al.* (2012) (red). HZF, high Zagros fault; IZ, imbricated zone; MFF, main frontal fault; MZF, main Zagros fault; SSZ, Sanandaj Sirjan zone; UDMA, Urumieh Dokhtar Magmatic Arc; ZFTB, Zagros fold-and-thrust belt.

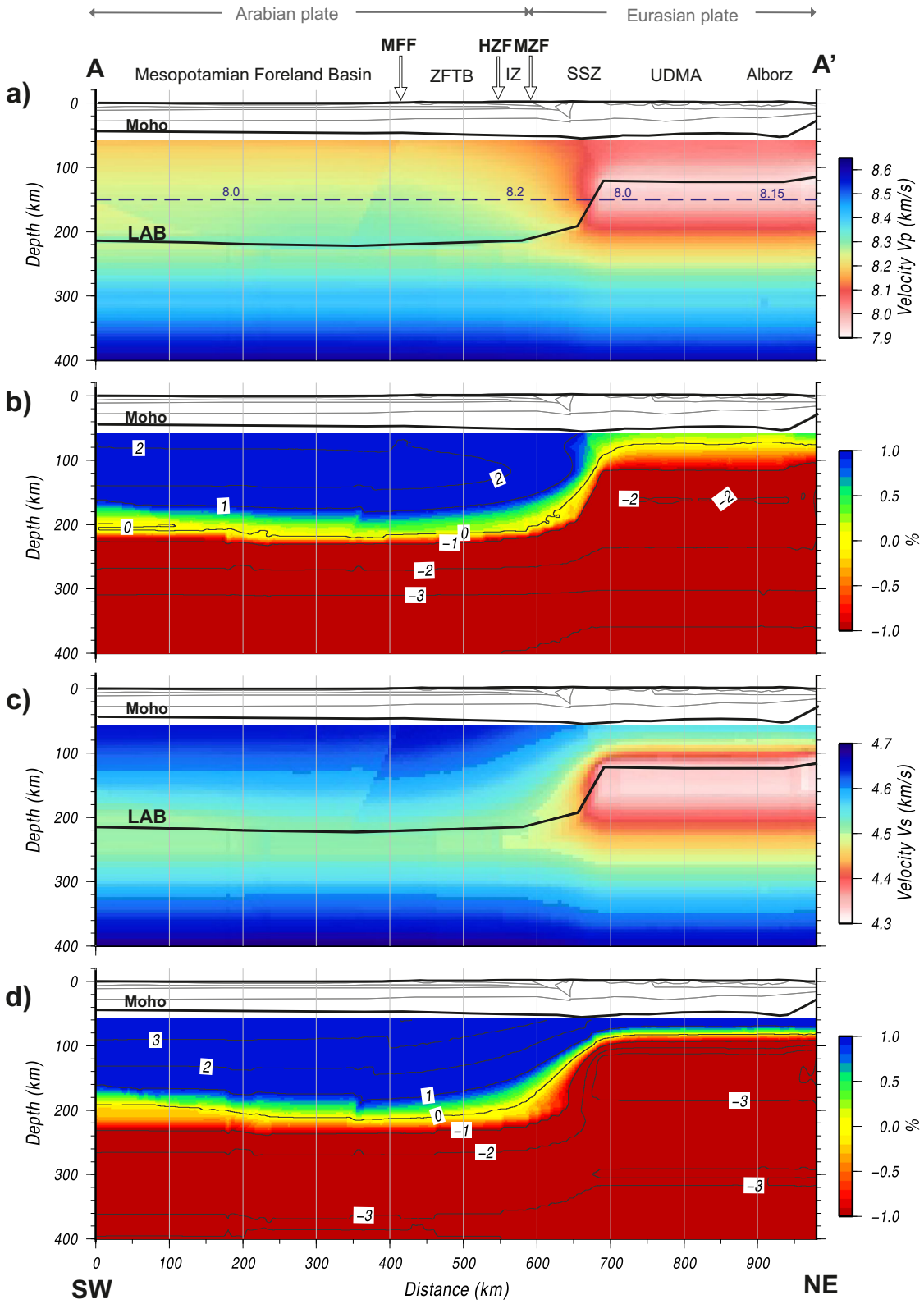

Figure 9. A–A′ profile. (a) *P*-wave mantle velocity distribution; (b) *P*-wave seismic velocity anomaly with respect to AK135 reference velocity model (Kennett *et al.* 1995); (c) *S*-wave mantle velocity distribution and (d) *S*-wave seismic velocity anomaly with respect to AK135 reference velocity model (Kennett *et al.* 1995). Numbers along dashed line represent velocity values from tomography model by Simmons *et al.* (2011).

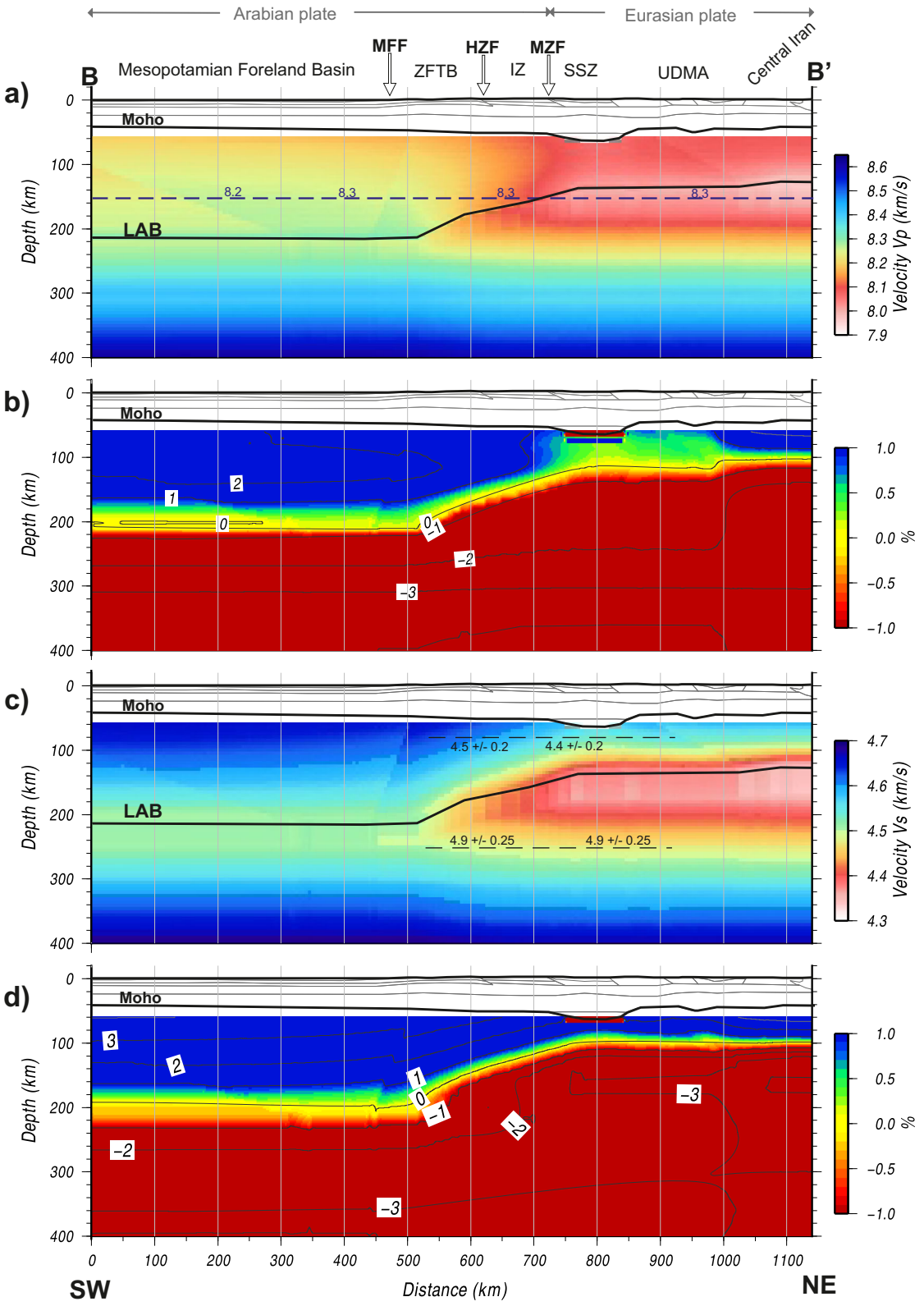

Figure 10. B–B′ profile. (a) *P*-wave mantle velocity distribution; (b) *P*-wave seismic velocity anomaly with respect to AK135 reference velocity model (Kennett *et al.* 1995); (c) *S*-wave mantle velocity distribution; (d) *S*-wave seismic velocity anomaly with respect to AK135 reference velocity model (Kennett *et al.* 1995). Numbers along dashed blue (panel a) and black (panel c) lines represent velocity values from tomography model by Simmons *et al.* (2011) (a) and from Kaviani *et al.* (2007) (c), respectively.

Table 3 The RMSE between measurements and calculated data for the profiles A–A′ and B–B′ (see Figs 7 and 8) and test models (see the Appendix).

Profile	Reference to Table A1 in the Appendix	Bouguer anomaly (mGal)	Geoid (m)	Topography (m)
A–A′ (Fig. 7)		7.28	1.13	215.14
B–B′ (Fig. 8)		5.93	1.19	158.73
Archean lith. mantle (Fig. A1)	Mantle a	67.83	4.05	2736.50
Proterozoic lith. mantle (Fig. A1)	Mantle b	17.36	1.57	328.78
Phanerozoic lith. mantle (Fig. A1)	Mantle c	25.67	2.89	1047.54

in the distribution of seismic velocities is observed along profile B–B′ (Fig. 10) with small variations in the calculated *Vp* and *Vs* values. Low *Vp* and *Vs* velocities extend over a wider region than in profile A–A′ related to the lithospheric mantle thinning, although, the anomalies show a lesser amplitude due to composition effects.

6 DISCUSSION

The numerical experiments carried out in this study are based on the combination of petrology, mineral physics and geophysical observables, allowing for the self-consistent calculation of mantle physical parameters, such as density, thermal conductivity and seismic velocities and their related observables. At the same time, the incorporation of geological data and recently acquired seismic data reduced considerably the uncertainties inherent to previous lithospheric models in the region. In the Appendix, we discuss the sensitivity of our models to compositional variations within the lithospheric mantle.

6.1 Geophysical-petrological versus pure thermal approaches

A noteworthy result is that the density distributions obtained in this work differ considerably from those obtained from a pure thermal approach (e.g. Molinaro *et al.* 2005; Motavalli-Anbaran *et al.* 2011; Jiménez-Munt *et al.* 2012). In the pure thermal approach, the density of the lithospheric mantle depends only on temperature, such that $\rho_m(z) = \rho_a\ [1 + \alpha\ (T_a - T(z))]$, where $\rho_a = 3200$ kg m^{-3} and $T_a = 1330$ °C are the density and temperature of the asthenosphere, respectively, and are constant everywhere, and $\alpha = 3.5 \times 10^{-5}$ °C^{-1} is the thermal expansion coefficient. Accordingly, the density in the subcrustal domain of the Mesopotamian Foreland Basin would vary from about 3300 kg m^{-3} at the crust–mantle boundary to 3200 kg m^{-3} in the LAB, keeping this value down to 400 km depth. Interestingly, despite the large differences in the density–depth distribution obtained from the two approaches, the corresponding lithospheric models show similar trends, in terms of lithospheric geometry. The reason for that is twofold: (1) On the one hand, although the resulting lithospheric mantle density from the geophysical-petrological approach is, considerably, higher than that from the pure thermal approach, calculated elevations are comparable, because both approaches use different reference columns to calculate the lithospheric buoyancy. In the pure thermal approach the reference column is the lithosphere at mid-oceanic ridges, with a constant sublithospheric density of $\rho_a = 3200$ kg m^{-3} (e.g. Lachenbruch & Morgan 1990). In the geophysical-petrological approach, the reference column is also the lithosphere at mid-oceanic ridges, but in this case, the sublithospheric mantle extends down to 400 km depth and the mantle density is calculated according to its composition and *P–T* conditions; (2) On the other hand, the similarity in calculated elevations indicates that the predominant effect on lateral density variations is related to temperature rather than pressure and, in our case, composition.

As discussed later, although the results from our modelling are comparable with previous models, they show conspicuous differences in the crustal structure and LAB depth. Major differences in the crustal structure and Moho depth are encountered, with respect to the works by Molinaro *et al.* (2005) and Motavalli-Anbaran *et al.* (2011), partly, because these authors use a very simplified upper crust structure and different density contrasts. However, the obtained LAB depths do not differ much, except with respect to the location and sharpness of the mantle thinning. The modelling approach used by Jiménez-Munt *et al.* (2012) is remarkably simpler, since calculations are performed in 1-D and both the crust and the lithospheric mantle are considered as homogeneous layers. Despite this simplicity, the main trends of Moho and LAB geometries are fairly reproduced although notable differences in the obtained values and short wavelength features were found.

6.2 Crustal geometry

The incorporation of geological cross-sections, based on geological field data along our modelled transects gives a better resolution on the shallow crustal structure. In addition, the significant amount of recent seismic experiments, allowed us to fairly constrain the Moho depth, by modifying the relative thickness of upper-middle crust and lower crust to simultaneously fit all the geophysical observables. Fig. 6 displays the crust–mantle boundary inferred from previous studies, showing differences in crustal thickness exceeding 10 km among different authors and methods. Our crustal model along transect A–A′ shows a crustal thickness of 42–43 km below the Arabian Foreland Basin, gradually increasing towards the Zagros Mountains. These values are similar to those proposed by Gök *et al.* (2008) and Nasrabadi *et al.* (2008). Maximum crustal thicknesses are obtained beneath the SSZ (55 km) and the Alborz Mountains (53 km) in good agreement with Paul *et al.* (2010) and Nasrabadi *et al.* (2008). Large discrepancies are obtained in the Alborz Mountains, relative to crustal thickness values proposed by Sodoudi *et al.* (2009), who proposed crustal thickness values up to 70 km. Along the B–B′ transect, the Arabian Foreland Basin shows a similar crustal thickness to that in the northern transect, with values exceeding those proposed by Alinaghi *et al.* (2007), by 4–7 km. Across the Zagros and Central Iran, our results show a good agreement with previous studies. Major discrepancies are found below the SSZ where Paul *et al.* (2010) propose a maximum crustal thickness of 69 km, in contrast to 63 km, as inferred from our model. This exceptional crustal thickening is restricted to a region of ∼150 km in width, and displaced relative to the higher elevations of the IZ. Nevertheless, seismic data in this region show larger uncertainties than other areas, due to the lack of seismic stations and the consequent poor ray coverage (Paul *et al.* 2006). Note that, obtaining a very thick crust in this region requires considering a

completely eclogitized lower crustal body, in order to simulate densities similar to the uppermost mantle. If this body is not considered, the modelled Moho depth is of ∼53 km, in good agreement to the values proposed by Manaman *et al.* (2011) from seismic data, and Molinaro *et al.* (2005) and Motavalli-Anbaran *et al.* (2011) from modelling. Slight discrepancies in resulting Moho depth values are found also between different receiver function studies (i.e. in the Alborz along A–A′ profile, in the UDMA and IZ along the B–B′ profile). In general, along both transects, our resulting Moho depth values are consistent with the results from Gök *et al.* (2008), which found ∼42–45 km of crustal thickness in the Foreland Basin, from Gritto *et al.* (2008), which calculated Moho depth values between 44 and 52 km in the NW Zagros, and from Radjaee *et al.* (2010), which found ∼55 km below the Zagros Mountains and 53–58 km below the Alborz Mountains. Our values of Moho depth differ slightly from those proposed by Jimenez-Munt *et al.* (2012), being 3–5 km higher along profile A–A′ (Fig. 7) and practically coincident along profile B–B′ (Fig. 8).

6.3 LAB geometry and compatibility with tomography models

Numerous studies have highlighted the lower *P*- and *S*-wave velocities and the higher attenuation of *Pn* and *Sn* waves, below Central Iran and/or the internal parts of the Zagros Mountains, relative to the adjacent Arabian Platform (Villaseñor *et al.* 2001; Ritzwoller *et al.* 2002; Maggi & Priestley 2005; Kaviani *et al.* 2007; Manaman & Shomali 2010; Agard *et al.* 2011; Vergés *et al.* 2011). Low velocities and high attenuation are, usually, interpreted as implying relatively high temperatures. Our resulting lithospheric mantle geometry depicts a pronounced lithospheric thinning from about 215 km in the Arabian Platform to 125–130 km in the UDMA and Central Iran along both profiles. This lithospheric thinning has also been proposed in former lithospheric models (e.g. Molinaro *et al.* 2005; Motavalli-Anbaran *et al.* 2011; Jiménez-Munt *et al.* 2012). A main difference with these models is the location and sharpness of the lithospheric thinning. Profile A–A′ shows similar results to those of Motavalli-Anbaran *et al.* (2011), in terms of sharpness but, in our model, lithospheric thinning occurs about 100 km farther to the NE. The location of this abrupt LAB rising in our model is the result of the best fit of all the geophysical observables in the region, including the location of the positive-negative velocity anomaly transition imaged in the tomography of Fig. 4(a). Differences with respect to the LAB geometry, proposed by Jiménez-Munt *et al.* (2012), are clear in both LAB and sharpness of lithospheric thinning (Fig. 8). Prominent differences also appear when comparing our results along profile B–B′ to those obtained by Molinaro *et al.* (2005) along a profile located 250 km further SE. According to these authors, the lithosphere thins very sharply from 210 km to about 100 km over a <80 km wide region beneath the main frontal fault, increasing steadily to values of 140 km beneath Central Iran. The lithospheric structure along B–B′ proposed by Jiménez-Munt *et al.* (2012) shows a smoother lithospheric thinning, in terms of sharpness and a ∼20 km thicker lithosphere beneath UDMA and Central Iran (Fig. 8).

Caution must be taken when comparing calculated seismic velocities with tomography models and our calculated velocities should only be qualitatively compared to tomography models. High velocities beneath the ZFTB are also observed in the tomography model by Manaman & Shomali (2010), obtained by using the partitioned waveform inversion method. In this case, the authors used an *ad hoc* regional reference model with low velocities characterizing the lithospheric mantle below the UDMA and towards Central Iran, whereas, the highest velocities mark the lithosphere below the ZFTB and the foreland basin. This strong velocity contrast at 100–150 km depth, close to the suture zone, is also observed in other surface and body wave tomography studies (e.g. Villaseñor *et al.* 2001; Maggi & Priestley 2005; Alinaghi *et al.* 2007; Kaviani *et al.* 2007). Our results are also in agreement with the absolute values of *Vs*, as calculated by Kaviani *et al.* (2007) in central Zagros (Fig. 10c), who, in reproducing a decrease in the shear wave velocity values towards the Central Iran, found a low velocity zone, immediately below the Moho in the SSZ. A further discussion is required when comparing our results with the recent tomography model by Simmons *et al.* (2011). These authors show high *Vp* values (8.3 km s^{-1}) below the ZFTB and IZ, and also below the UDMA (Fig. 10a), allowing for the interpretation of the Arabian Plate underthrusting the Eurasian lithosphere. Though our calculated seismic velocities in the same region (at 150 km depth) are lower than those proposed in Simmons *et al.* (2011; Fig. 10a), we do not obtain any lithospheric-scale underthrusting feature when converting the calculated *Vp* values into ΔVp (%), relative to the AK135 reference model.

Finally, receiver function studies (Hansen *et al.* 2007; Mohammadi *et al.* 2013) show different LAB depth values, relative to those obtained in our models, indicating a shallower LAB in the whole area (∼160 km depth in the Arabian Platform, ∼130 km depth beneath the ZFTB, ∼150 km beneath the SSZ and 80–85 km in Central Iran). This discrepancy could be due to a misinterpretation of the horizon detected by receiver functions which, as suggested in a recent work by Yuan & Romanowicz (2010), probably corresponds to the sharp mid-lithosphere boundary, rather than to the more gradual LAB. Alternatively, as noted by Eaton *et al.* (2009), the definition of LAB depends on the observation method and, therefore, the thermal and seismic LABs are not forced to coincide.

7 CONCLUDING REMARKS

We have presented new lithospheric models along two transects across the Arabia–Eurasia Plate boundary, combining geological, geophysical and petrological data within an internally consistent thermodynamic-geophysical framework. The approach allows calculations of absolute elevation, gravity anomaly, geoid height, surface heat flow and mantle seismic velocities and their comparisons with observations. The results obtained in this study allow us to make the following concluding remarks:

(i) Our model reproduces the general trends of the Moho topography, obtained from previous seismic experiments reducing the uncertainties associated with the gathering of data with different provenance and regions with poor or null data coverage. A highly eclogitized lower crust beneath the SSZ is required (central Zagros).

(ii) The obtained LAB geometries reproduce a pronounced lithospheric mantle thinning from the Arabian to the Eurasian lithosphere in agreement with tomography and previous lithosphere models. However, conspicuous differences in terms of depth to the LAB, and sharpness and location of the lithospheric mantle thinning are encountered between the two selected profiles.

(iii) Lateral changes in the composition of the lithospheric mantle are required to reproduce *P*- and *S*-wave seismic velocities from tomography models. Our results are compatible with a Proterozoic lherzolitic composition beneath the Arabian Platform, changing progressively to a more enriched composition beneath the Mesopotamian Foreland Basin and the Persian Gulf, and below the

accreted terrains of the Eurasian Plate (Urumieh Dokhtar Magmatic Arc and Central Iran). Below the ZFTB and the IZ, a more depleted Phanerozoic harzburgitic-type mantle composition has been considered.

(iv) Along-strike variations of the lithosphere structure are, mainly, related to the region where the lithospheric thinning occurs. In the NW Zagros region (Lurestan, profile A–A′) lithospheric thinning is very sharp and located beneath the SSZ, coinciding with the Arabian-Eurasian Plate suture (the MZF). In the central Zagros region (Fars, profile B–B′) lithospheric thinning is smoother and affects a wide region of the NE-Arabian Plate, including the ZFTB and the IZ.

ACKNOWLEDGEMENTS

This study is a contribution of the Group of Dynamics of the Lithosphere (GDL) within the framework of the following projects: ATIZA (CGL2009–09662-BTE), TopoMed/GASAM (CGL2008–03474-E/BTE/07-TOPO-EUROPE-FP-006), TopoIberia-Consolider Ingenio 2010 (CSD2006–00041), TECLA (CGL2011–26670) and DARIUS Programme and its sponsors. We would like to thank J.C. Afonso for helpful discussions on mantle composition and thermodynamics. Constructive reviews from Jörg Ebbing and another anonymous reviewer and the advices of the Editor Dan Shim, largely improved the final version of the manuscript.

REFERENCES

Afonso, J.C. & Zlotnik, S., 2011. The subductability of the continental lithosphere: the before and after story, in Arc-continent collision, in *Frontiers in Earth Sciences,* pp. 53–86, eds Brown, D. & Ryan, P.D., Springer.

Afonso, J.C., Fernàndez, M., Ranalli, G., Griffin, W.L. & Connolly, J.A.D., 2008. Integrated geophysical-petrological modeling of the lithosphere and sub-lithospheric upper mantle: methodology and applications, *Geochem. Geophys. Geosyst.,* **9,** Q05008, doi:10.1029/2007GC001834.

Afonso, J.C., Fullea, J., Griffin, W.L., Yang, Y., Jones, A.G., Connolly, J.A.D. & O'Reilly, S.Y., 2013a. 3-D multi-observable probabilistic inversion for the compositional and thermal structure of the lithosphere and upper mantle, I: a priori petrological information and geophysical observables, *J. geophys. Res.,* **118,** 2586–2617.

Afonso, J.C., Fullea, J., Yang, Y., Connolly, J.A.D. & Jones, A.G., 2013b. 3-D multi-observable probabilistic inversion for the compositional and thermal structure of the lithosphere and upper mantle, II: general methodology and resolution analysis, *J. geophys. Res.,* **118,** 1650–1676.

Agard, P. *et al.*, 2011. Zagros orogeny: a subduction-dominated process, *Geol. Mag.,* **148**(5–6), 692–725.

Alinaghi, A., Kolakov, I. & Thybo, H., 2007. Seismic tomographic imaging of P- and S-waves velocity perturbations in the upper mantle beneath Iran, *Geophys. J. Int.,* **169,** 1089–1102.

Allen, M., Ghassemi, M.R., Shahrabi, M. & Qorashi, M., 2003. Accommodation of late Cenozoic oblique shortening in the Alborz range, northern Iran, *J. Struct. Geol.,* **25**(5), 659–672.

Amante, C. & Eakins, B.W., 2009. ETOPO1 arc-minute global relief model: procedures, data sources and analysis, NOAA Technical Memorandum NESDIS NGDC-24, 19 pp. Available at: http://www.ngdc.noaa.gov.

Artemieva, I.M, 2006. Global 1 × 1 thermal model TC1 for the continental lithosphere: implications for lithosphere secular evolution, *Tectonophysics,* **426,** 245–277.

Berberian, M. & King, G.C.P., 1981. Towards a palegeography and tectonic evolution of Iran, *Can. J. Earth Sci.,* **18,** 210–265.

Bijwaard, H., Spakman, W. & Enghdal, E.R., 1998. Closing the gap between regional and global travel time tomography, *J. geophys. Res.,* **103,** 30 055–30 078.

Bird, P., 1978. Finite element modeling of lithosphere deformation: the Zagros collision orogeny, *Tectonophysics,* **50,** 307–336.

Casciello, E., Vergés, J., Saura, E., Casini, G., Fernández, N., Blanc, E., Homke, S. & Hunt, D., 2009. Fold patterns and multilayer rheology of the Lurestan Province, Zagros Simply Folded Belt (Iran), *Geol. Soc. Lond.,* **166,** 1–13.

Connolly, J., 2005. Computation of phase equilibria by linear programming: a tool for geodynamic modeling and an application to subduction zone decarbonation, *Earth planet. Sci. Lett.,* **236,** 524–541.

Eaton, D.W., Darbyshire, F., Evans, R.L., Grütter, H., Jones, A.G. & Yuan, X., 2009. The elusive lithosphere-asthenosphere boundary (LAB) beneath cratons, *Lithos,* **109,** 1–22.

Egan, S.S., Mosar, J., Brunet, M.-F. & Kangarli, T., 2009. Subsidence and uplift mechanisms within the South Caspian Basin: insights from the onshore and offshore Azerbaijan region, *Geol. Soc. Spec. Publ.,* **312,** 219–240.

Emami, H., Vergés, J., Nalpas, T., Gillespie, P., Sharp, I., Karpuz, R., Blanc, E.J.-P. & Goodarzi, M.G.H., 2010. Structure of the Mountain Front Flexure along the Anaran anticline in the Pusht-e Kuh Arc (NW Zagros, Iran): insights from sand box models, in *Tectonic and Stratigraphic Evolution of Zagros and Makran during the Mesozoic-Cenozoic,* pp. 155–78, eds Leturmy, P. & Robin, C., Geol. Soc. London Spec. Pub. no. 330.

Engdahl, E.R., Van der Hilst, R.D. & Buland, R.P., 1998. Global teleseismic earthquake relocation with improved travel times and procedures for depth determination, *Bull. seism. Soc. Am.,* **88**(3), 722–743.

Förster, A., Förster, H.J., Masarweh, R., Masri, A. & Tarawneh, K., 2007. The surface heat flow of the Arabian Shield in Jordan, *J. Asian Earth Sci.,* **30,** 271–284.

Fullea, J., Fernàndez, M. & Zeyen, H., 2008. FA2BOUG - A FORTRAN 90 code to compute Bouguer gravity anomalies from gridded free-air anomalies: application to the Atlantic-Mediterranean transition zone, *Comput. Geosci.,* **34**(12), 1665–1681.

Fullea, J., Afonso, J.C., Connolly, J.A.D, Fernández, M., García-Castellanos, D. & Zeyen, H., 2009. LitMod 3D: an interactive 3D software to model the thermal, compositional, density, seismological, and rheological structure of the lithosphere and sublithospheric upper mantle, *Geochem., Geophys., Geosystem,* **10**(8), doi: 10.129/2009GC002391.

Ghasemi, A. & Talbot, C.J., 2006. A new tectonic scenario for the Sanandaj Sirjan Zone (Iran), *J. Asian Earth Sci.,* **26,** 683–693.

Gök, R., Mahdi, H., al-Shukri, H. & Rodgers, A., 2008. Crustal structure of Iraq from receiver functions and surface wave dispersion; implications for understanding the deformation history of the Arabian-Eurasian collision, *Geophys. J. Int.,* **172,** 1179–1187.

Griffin, W., O'Reilly, S.Y., Abe, S.Y., Aulbach, N., Davies, S., Pearson, R.M., Doyle, N.J. & Kivi, B.J., 2003. The origin and evolution of Archean lithospheric mantle, *Precambrian Res.,* **127,** 19–41.

Griffin, W.L., O'Reilly, S.Y., Afonso, J.C. & Begg, G., 2009. The composition and evolution of lithospheric mantle: a re-evaluation and its tectonic implications, *J. Petrol.,* **50,** 1185–1204.

Gritto, R. *et al.*, 2008. Crustal structure of North Iraq from receiver function analyses, *Monitoring Research Review: Ground-Based Nuclear Explosion Monitoring Technologies,* **298,** 80–86.

Hansen, S.E., Rodgers, A.J., Schwartz, S.Y. & Al-Amri, A.M.S., 2007. Imaging ruptured lithosphere beneath the Red Sea and Arabian Peninsula, *Earth planet. Sci. Lett.*. **259,** 256–265.

Holland, T. & Powell, R., 1998. An internally consistent thermodynamic data set for phases of petrological interest, *J. Metamorph. Geol.,* **16,** 309–343.

Jiménez-Munt, I., Fernàndez, M., Saura, E., Vergés, J. & García-Castellanos, D., 2012. 3D lithospheric structure and regional/residual Bouguer anomalies from Arabia-Eurasia collision (Iran), *Geophys. J. Int.,* **190,** 1311–1324.

Kaviani, A., Paul, A., Bourova, E., Hatzfeld, D., Pedersen, H. & Mokhtari, M., 2007. A strong seismic velocity contrast in the shallow mantle across the Zagros collision zone (Iran), *Geophys. J. Int.,* **171,** 399–410.

Kennett, B.L.N., Engdahl, E.R. & Buland, R., 1995. Constraints on seismic velocities in the Earth from travel times, *Geophys. J. Int.,* **122,** 108–124.

Lachenbruch, A.H. & Morgan, P., 1990. Continental extension, magmatism and elevation: formal relations and rules of thumb, *Tectonophysics,* **174,** 39–62.

Lucazeau, F., Leroy, S., Rolandone, F., d'Acremont, E., Watremez, L., Bonneville, A., Goutorbe, B. & Düsünur, D., 2010. Heat-flow and hydrothermal circulation at the ocean-continent transition of the eastern Gulf of Aden, *Earth planet. Sci. Lett.,* **295,** 554–570.

Maggi, A. & Priestley, K., 2005. Surface waveform tomography of the Turkish–Iranian plateau, *Geophys. J. Int.,* **160,** 1068–1080.

Manaman, N.S. & Shomali, H., 2010. Upper mantle S-velocity structure and Moho depth variations across Zagros belt, Arabian–Eurasian plate boundary, *Phys. Earth planet. Int.,* **180,** 92–103.

Manaman, N.S., Shomali, H. & Koyi, H., 2011. New constraints on uppermantle S-velocity structure and crustal thickness of the Iranian plateau using partitioned waveform inversion, *Geophys. J. Int.,* **184,** 247–267.

McDonough, W.F. & Sun, S., 1995. The composition of the Earth, *Chem. Geol.,* **120,** 223–253.

McQuarrie, N., 2004. Crustal scale geometry of the Zagros fold-thrust belt, Iran, *J. Struct. Geol.,* **26,** 519–535.

McQuarrie, N. & van Hinsbergen, D.J.J., 2013. Retro-deforming the Arabia-Eurasia collision zone: age of collision versus magnitude of continental subduction, *Geology,* **41,** 315–318.

Mohammadi, N., Sodoudi, F., Mohammadi, E. & Sadidkhouy, A., 2013. New constraints on lithospheric thickness of the Iranian plateau using converted waves, *J. Seismol.,* **17,** 883–895.

Molinaro, M., Zeyen, H. & Laurencin, X., 2005. Lithospheric structure beneath the southeastern Zagros Mountains, Iran: recent slab break-off?, *Terra Nova,* **17,** 1–6.

Morley, C.K. *et al.*, 2009. Structural development of a major late Cenozoic basin and transpressional belt in central Iran: the Central Basin in the Qom-Saveh area, *Geosphere,* **5**(4), 325–362.

Motavalli-Anbaran, S.-H., Zeyen, H., Brunet, M.-F. & Ardestani, V.E., 2011. Crustal and lithospheric structure of the Alborz Mountains, Iran, and surrounding areas from integrated geophysical modeling, *Tectonics,* **30,** TC5012, doi:10.1029/2011TC002934.

Mouthereau, F., Tensi, J., Bellahsen, N., Lacombe, O., De Boisgrollier, T. & Kargar, S., 2007. Tertiary sequence of deformation in a thin-skinned/thick-skinned collision belt: the Zagros Folded Belt (Fars, Iran), *Tectonics,* **26,** TC5006, doi:10.1029/2007TC002098.

Mouthereau, F., Lacombe, O. & Vergés, J., 2012. Building the Zagros collisional orogen: timing, strain distribution and the dynamics of Arabia/Eurasia plate convergence, *Tectonophysics,* **532–535,** 27–60.

Nasrabadi, A., Tatar, M., Priestley, K. & Sepahvand, M.R., 2008. Continental lithosphere structure beneath the Iranian plateau, from analysis of receiver functions and surface waves dispersion, in *Proceedings of the 14th World Conference on Earthquake Engineering,* 2008 October 12–17, Beijing, China.

Nowrouzi, G., Ghafoury, M., Ashtiany, M. & Javan Doley, G., 2007. Crustal velocity structure of northeast of central Iran and Binalud zone, using teleseismic receiver functions, *J. Earth Space Phys.,* **33,** 1205–8647.

O'Reilly, S.Y. & Griffin, W.L., 2006. Imaging chemical and thermal heterogeneity in the sub-continental lithospheric mantle with garnets and xenoliths. Geophysical implications, *Tectonophysics,* **416,** 289–309.

Paul, A., Kaviani, A., Hatzfeld, D., Vergne, J. & Mokhtari, M., 2006. Seismological evidence for crustal-scale thrusting in the Zagros mountain belt (Iran), *Geophys. J. Int.,* **166,** 227–237.

Paul, A., Hatzfeld, D., Kaviani, A., Tatar, M. & Péquegnat, C., 2010. Seismic imaging of the lithospheric structure of the Zagros mountain belt (Iran), *Geol. Soc. Lond., Spec. Pub.,* **330,** 5–18.

Pavlis, N.K., Holmes, S.A., Kenyon, S.C. & Factor, J.K., 2008. An earth gravitational model to degree 2160: EGM2008, in *Proceedings of the 2008 General Assembly of the European Geosciences Union,* Vienna, Austria, 2008 April 13–18, EGU2008-A-01891.

Pollack, H.N., Hurter, S.J. & Johnson, J.R., 1993. Heat-Flow from the Earth's interior-analysis of the global data set, *Rev. Geophys.,* **31,** 267–280.

Poudjom-Djomani, Y.H., O'Reilly, S.Y., Griffin, W.L. & Morgan, P., 2001. The density structure of subcontinental lithosphere through time, *Earth planet. Sci. Lett*., **184,** 605–621.

Radjaee, A., Rham, D., Mokhtari, M., Tatar, M., Priestley, K. & Hatzfeld, D., 2010. Variation of Moho depth in the central part of the Alborz Mountains, northern Iran, *Geophys. J. Int.,* **181,** 173–184.

Ritzwoller, M.H., Shapiro, N.M., Barmin, M.P. & Levshin, A.L., 2002. Global surface wave diffraction tomography, *J. geophys. Res.,* **107**(B12), 2335, doi:10.1029/2002JB001777.

Rolandone, F., Lucazeau, F., Leroy, S., Mareschal, J.-C., Jorand, R., Goutorbe, B. & Bouquerel, H., 2013. New heat flow measurements in Oman and the thermal state of the Arabian Shield and Platform, *Tectonophysics,* **589,** 77–89.

Sandwell, D.T. & Smith, H.W.F., 1997. Marine gravity anomalies from GEOSAT and ERS-1 satellite altimetry, *J. geophys. Res.,* **102,** 10 039–10 054.

Sengör, A.M.C., Altiner, D., Cin, A., Ustaomer, T. & Hsu, K.J., 1988. Origin and assembly of the Tethyside orogenic collage at the expense of Gondwana Land, *Geol. Soc. Lond., Spec. Pub.* **37,** 119–181.

Sepehr, M. & Cosgrove, J.W., 2004. Structural framework of the Zagros fold-thrust belt, Iran, *Mar. Petrol. Geol.,* **21**(7), 829–843.

Sherkati, S., Letouzey, Y. & Frizon de Lamotte, D., 2006. Central Zagros fold-thrust belt (Iran): new insights from seismic data, field observation and sandbox modeling, *Tectonics,* **25,** TC4007, doi:10.1029/2004TC001766.

Shervais, J.W., 2001. Birth, death, and resurrection: the life cycle of suprasubduction zone ophiolites, *Geochem. Geophys. Geosyst.,* **2,** 1525–2027.

Shomali, Z.H., Keshvari, F., Hassanzadeh, J. & Mirzaei, N., 2011. Lithospheric structure beneath the Zagros collision zone resolved by non-linear teleseismic tomography, *Geophys. J. Int.,* **187**(1), 394–406.

Simmons, N.A., Myers, S.C. & Johannesson, G., 2011. Global-scale P wave tomography optimized for prediction of teleseismic and regional travel times for Middle East events: 2. Tomographic inversion, *J. geophys. Res.* **116,** B04305, doi:10.1029/ 2010jb007969.

Snyder, D.B. & Barazangi, M., 1986. Deep crustal structure and flexure of the Arabian Plate beneath the Zagros collisional mountain belt as inferred from gravity observations, *Tectonics,* **5**(3), 361–373.

Sodoudi, F., Yuan, X., Kind, R., Heit, B. & Sadidkhouy, A., 2009. Evidence for a missing crustal root and a thin lithosphere beneath the Central Alborz by receiver function studies, *Geophys. J. Int.,* **177,** 733–742.

Stern, R.J. & Johnson, P., 2010. Continental lithosphere of the Arabian plate: a geologic, petrologic, and geophysical synthesis, *Earth Sci. Rev.,* **101,** 29–67.

Su, B-X. *et al.*, 2014. Composition and structure of the lithospheric mantle beneath NE-Iran: constraints from mantle xenoliths, *Lithos,* **202–203,** 267–282.

Vergés, J., Saura, E., Casciello, E., Fernàndez, M., Villaseñor, A., Jiménez-Munt, I. & García-Castellanos, D., 2011. Crustal-scale cross-section across the NW Zagros Belt: implications for the Arabian Margin reconstruction, *Geol. Mag.*, **148,** 739–761.

Villaseñor, A., Ritzwoller, M.H., Levshin, A.L., Barmin, M.P., Engdahl, E.R., Spakman, W. & Trampert, J., 2001. Shear velocity structure of central Eurasia from inversion of surface wave velocities, *Phys. Earth planet. Int.,* **123,** 169–184.

Villaseñor, A., Spakman, W. & Engdahl, E.R., 2003. Influence of regional travel times in global tomographic models, *Geophys. Res. Abstr.,* **5,** Abstract, EAE03-A-08614, EGS-AGU-EUG Joint Assembly, Nice.

Yuan, H. & Romanowicz, B., 2010. Lithospheric layering in the North American craton, *Nature,* **466,** 1063–1068.

Zeyen, H. & Fernàndez, M., 1994. Integrated lithospheric modeling combining thermal, gravity, and local isostasy analysis: application to the NE Spanish Geotransect, *J. geophys. Res.,* **99,** 18 089–18 102.

Zeyen, H., Ayarza, P., Fernàndez, M. & Rimi, A., 2005. Lithospheric structure under the western African-European plate boundary: a transect across the Atlas Mountains and the Gulf of Cadiz, *Tectonics,* **24,** TC2001, doi:10.1029/2004TC001639.

APPENDIX: LATERAL VARIATIONS IN LITHOSPHERIC MANTLE COMPOSITION

Considering a compositionally homogeneous lithospheric mantle, we performed a number of tests along profile A–A′ changing the mantle chemical composition in order to check the sensitivity of the model to lateral variations in lithospheric mantle composition. Crustal structure (geometry and parameters) and LAB geometry are fixed. Fig. A1 shows the obtained results along profile A–A′, by considering compositions corresponding to Archean, Proterozoic and Phanerozoic lithospheric mantles (Table A1). The corresponding misfits between measured and calculated data are reported in Table 3. As expected, the Archean lithospheric mantle composition results in a considerable uplift of the whole region, since it is highly depleted in incompatible elements (Al, Ca and Fe) and, therefore, is more buoyant. The calculated elevation exceeds the observed elevation by ∼3000 m in the Foreland Basin, ∼2000 km in the Zagros fold-and-thrust belt and ∼1500 m in the Eurasian part of the profile. The Phanerozoic lithospheric mantle composition is enriched in FeO, CaO and Al_2O_3 and depleted in MgO, which results in a higher density. This composition fits, quite well, the elevations in the UDMA and Alborz Mountains, whereas, it generates an increasing misfit towards the Arabian Foreland Basin, where the calculated topography is ∼1000 m lower than observed. The best fit is obtained with a Proterozoic mantle composition, which is characterized by an intermediate depletion degree between Archean and

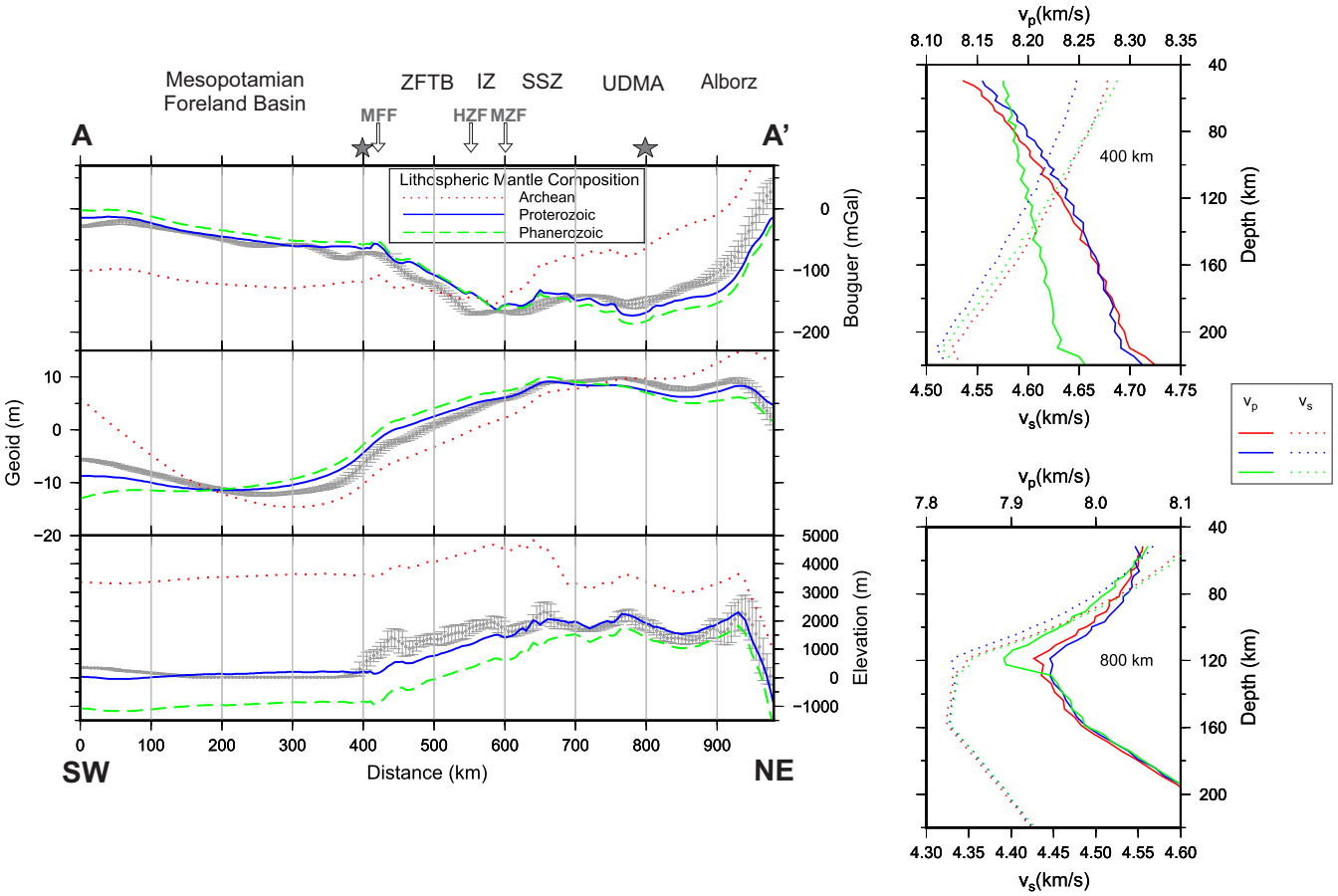

Figure A1. Calculated Bouguer and geoid anomalies, elevation, and seismic velocities for different lithospheric mantle compositions (Archean, Protherozoic and Phanerozoic) along A–A′ profile. Grey dots with error bars indicate the geophysical observables. Velocity profiles are calculated at 400 km (top right) and 800 km (bottom right) from the beginning of the profile.

Table A1 Chemical compositions used in test models for mantle bodies (Fig. A1).

Mantle compositions in the NCFMAS system (%)				
	Mantle a Arc1 Average Archean (Griffin *et al.* 2009)	Mantle b Pr6 Proterozoic (Griffin *et al.* 2009)	Mantle c Tc1 Average Phanerozoic (Griffin *et al.* 2009)	Asthenosphere–PUM Primitive Upper Mantle (McDonough & Sun 1995)
SiO_2	45.7	45.4	44.5	45
Al_2O_3	0.99	3.7	3.5	4.5
FeO	6.4	8.3	8.0	8.1
MgO	45.5	39.9	39.8	37.8
CaO	0.59	3.2	3.1	3.6
Na_2O	0.07	0.26	0.24	0.25
Total	99.25	100.76	96.05	99.25

Phanerozoic compositions, although, being highly enriched in FeO. However, a misfit of ∼500 m in elevation is found in the Zagros fold-and-thrust belt and the IZ. Bouguer and geoid height anomalies reveal the same mass excess/deficit as elevation. Fitting the observables with a homogeneous Proterozoic composition would require a notable thinning of the lithospheric mantle beneath the ZFTB and the resulting seismic velocities would be in disagreement with tomographic models.

Furthermore, we calculated the *P*- and *S*-wave velocity–depth distributions for each composition at 400 and 800 km distance from the beginning of the profile, corresponding to the Arabian and Eurasian lithospheric mantles, respectively. Calculated *Vp* ranges are from 8.12 to 8.30 km s^{-1} in the thick Arabian lithospheric mantle, and from 7.9 to 8.05 km s^{-1} in the thin lithospheric mantle beneath the magmatic arc. Similarly, *Vs* is in the range between 4.50 and 4.70 km s^{-1} in the Arabian lithospheric mantle, and from 4.33 to 4.60 km s^{-1}, in both locations, respectively. Interestingly, calculated *Vp* for Archean and Proterozoic compositions are similar but differ notably for Phanerozoic compositions. In turn, calculated Vs are similar for Archean and Phanerozoic and differ for Proterozoic compositions.These results show that lithospheric mantle density is particularly sensitive to the chosen bulk compositions, resulting in important variations in the calculated gravity and geoid anomalies and absolute elevation. The calculated seismic velocities appear to be more sensitive to lateral temperature variations (lithospheric thickness variations) than to the selected compositional variations.It must be noted, however, that identifying mantle density with bulk composition and seismic velocities is a difficult problem, due to the lack of uniqueness. Recent works by Afonso *et al.* (2013a,b), based on a non-linear 3-D multi-observable probabilistic (Bayesian) inversion approach, show that a wide range of compositions can, equally well, explain multiple geophysical data. Hence, deep temperature anomalies $\leq 150\,^{\circ}C$ and compositional anomalies $\Delta Mg\# < 3$ are not simultaneously resolvable, being that bulk Al_2O_3 content is a better compositional indicator than Mg#. In consequence, the considered mantle chemical compositions are compatible with the geophysical observables, but it would be difficult to decide whether these compositions are unique.